Thermal structure of the mantle beneath the equatorial Mid-Atlantic Ridge: Inferences from the spatial variation of dredged basalt glass compositions

J.-G. Schilling,[1] C. Ruppel,[2] A. N. Davis,[3] B. McCully,[1] S. A. Tighe,[1] R. H. Kingsley,[1] and J. Lin[4]

Abstract. We report on the major element composition of basaltic glasses from the Mid-Atlantic Ridge transecting the equatorial mega-fracture zones from 7°S to 5°N (65 stations, 10-20 km sampling intervals, 3.5 - 5 km water depth range). Many of the basaltic glasses are Na_2O, SiO_2, and MgO rich, similar to other basalt glasses erupted along the deepest regions of the mid-ocean ridge system, suggesting melt generation by relatively low degrees of partial melting at rather shallow depth in the upper mantle. Along the ridge axis, the compositional variations show regular and systematic long-wavelength trends with a major discontinuity at the complex St. Paul transform fault, just south of St. Peter and Paul islets. A corresponding long-wavelength trend in upper mantle potential temperature, mean pressure, and degree of melting and crustal thickness variation is inferred using parameterized petrologic decompression melting models. A 600-km-long, nearly linear negative gradient in these parameters is apparent from the Charcot fracture zone (FZ) to the St. Paul FZ. Over the length of this gradient, the upper mantle potential temperature drops by about 70°C, the mean degree of partial melting changes from 7% to 10%, and the inferred crustal thickness varies between 3 and 6 km. The gradient along the ridge axis is unaffected by the mega-transform fault offsets, implying that a broad (approximately 2000 km wide across-axis and 600 km long along-axis) cold zone is present in the upper mantle just south of the equator. At the discontinuity across the complex St. Paul transform fault, the gradients in inferred potential temperature, mean degree of partial melting, and crustal thickness abruptly change sign, respectively increasing by 80°C, rising from 7% to 10%, and changing from 3 to 6 km. The discontinuity is clearly related to the Sierra Leone plume affecting the Mid-Atlantic Ridge around 1.7°N, as also evident from Pb, Nd, and Sr isotopic variations previously reported on the same glasses (Schilling et al., 1994) and the K_2O variation reported here. The cause of the petrologically inferred cold zone and large gradient in the upper mantle south of St. Peter and Paul islets remains more speculative. On the basis of a passive mantle upwelling flow model (Phipps Morgan and Forsyth, 1988) applied to the specific geometry of the equatorial Atlantic, we reject the simplest hypothesis that the cold zone is produced by the compounding cooling effect caused by the very long and densely distributed transform fault offsets in the equatorial Atlantic. The result of this test remains paradoxical in view that good correlations exist between segment length, maximum along-ridge axis relief per segment, mean segment depth, and per segment average bulk compositions of the erupted basalts, and corresponding mean degrees of melting. Other possible causes for the gradational cold zone are briefly explored. These include the evolutionary history of the region with respect to adjacent continental mantle, lithosphere age, thickness, and temperature, and tectonic mode of opening of the Atlantic, as well as large-scale convective motion associated with continental dispersion. No definite conclusions can be reached. However, we emphasize that the petrologically inferred upper mantle thermal structure in the equatorial Atlantic is quite robust and independent of the petrologic decompression melting models considered and their underlying detailed assumptions. Large seismic S wave velocity variations are predicted over the 0-150 km depth range of the upper mantle, based on the reported correlation of Na_8 with S wave velocity reported by Yan et al. (1989). Thus detailed seismic tomographic mapping could be used to test further the cold upper mantle zone hypothesis for the equatorial Atlantic.

[1] Graduate School of Oceanography, University of Rhode Island, Narragansett.

[2] School of Earth and Atmospheric Sciences, Georgia Institute of Technology, Atlanta.

[3] Cameca Instrument Incorporated, Trumbull, Connecticut.

[4] Woods Hole Oceanographic Institution, Woods Hole, Massachusetts.

Introduction

It is generally accepted in plate tectonic theory that fracture zones may have profound effects on the thermal conditions and dynamics of mantle upwelling, the melting regime, the melt budget and the compositions of melt erupted along mid-ocean ridges [e.g., *Sleep and Biehler*, 1970; *Fox and Gallo*, 1984]. These transform fault effects (TFE) [*Phipps Morgan and Forsyth*, 1988] are manifested near ridge-transform fault intersections (RTI) by deepening of the elevation of the ridge axis

[*Forsyth and Wilson*, 1984; *Parmentier and Forsyth*, 1985], curving of the ridge axis [*Phipps Morgan and Forsyth*, 1988], and thinning of the oceanic crust [*White et al.*, 1984]. In a more complex way, TFE are also apparent in the gravity field as well [*Kuo and Forsyth*, 1988; *Prince and Forsyth*, 1988; *Lin et al.*, 1990]. TFE are also evident in along-axis changes in the composition of erupted basaltic melts and phenocrysts they contain. For example, lower derived melt temperatures [*Schilling and Sigurdsson*, 1979] and more evolved Fe-Ti rich basalts, which are often observed near RTIs, have been attributed to enhanced fractional crystallization at shallow depth [*Melson et al.*, 1967b; *Honnorez and Bonatti*, 1970; *Thompson and Melson*, 1972] and/or to a reduction in the extent of partial melting of the upwelling mantle resulting from these cold lithosphere edge effects [*Bender et al.*, 1984]. Occasional enhancement of incompatible trace element and isotope ratios in mid-ocean ridge basalts (MORB) erupted near RTIs, where low degrees of melting may prevail, have also been attributed to preferential melting of small ubiquitous mantle heterogeneity domains rich in volatiles, incompatible elements, and radiogenic Sr and Pb isotopes [*Langmuir and Bender*, 1984].

Although cold-edge effects near RTIs are now fairly well documented, their exact cause and controlling factors are not yet fully understood. These problems can profitably be further studied in the equatorial Atlantic where the Mid-Atlantic Ridge (MAR) is highly segmented and displaced en echelon left laterally by mega-transform faults (Figure 1). Age discontinuities across these transform faults range from a few million years up to 40-50 m.y. for the Romanche fracture zone (FZ) (Table 1), thus providing a means of evaluating the potential thermal effects of a wide range of transform fault lengths within a single spatially limited region. The bathymetry of this part of the mid-ocean ridge system may represent one manifestation of the thermal effects associated with the mega-transform offsets in the equatorial Atlantic. Most notably, the MAR axis reaches a maximum depth of 4-5 km at the equator where it is also most intensely segmented. Thus a legitimate question is whether the unusual depth of equatorial MAR reflects a mantle cold spot caused by the compounding of transform fault effects or is it due to some other causes. Also, the 3-5 km depth range of the equatorial MAR axis provides a critical window to test further the global correlation between ridge elevation and basalt chemistry pointed out by *Klein and Langmuir* [1987] and to evaluate further the implications of these correlations for the thermal and melting regime in the underlying mantle. Finally, the exposure of highly metasomatized, volatile, Sr and Pb radiogenic rich ultramafic mantle rocks on St. Peter and Paul's islets directly testifies to the presence of mantle heterogeneities [*Melson et al.*, 1967a; *Frey*, 1970; *Melson et al.*, 1972; *Melson and Thompson*, 1973; *Sinton*, 1979; *Roden et al.*, 1984]. The presence of the aseismic Ceara and Sierra Leone ridges, symmetrically distributed about the ridge axis just north of the equator (Figure 1), also suggests that a mantle plume might influence the MAR. The presence of such mantle heterogeneities and the numerous transform faults provides a means of testing further the model of preferential melting of ubiquitous mantle heterogeneities previously proposed by *Langmuir and Bender* [1984] and *Sleep* [1984].

For these reasons we undertook a systematic dredge sampling of glassy basalts along the axis of the MAR from 3°S to 5°N (Figure 1). The cruise took place in June-July 1987 aboard the
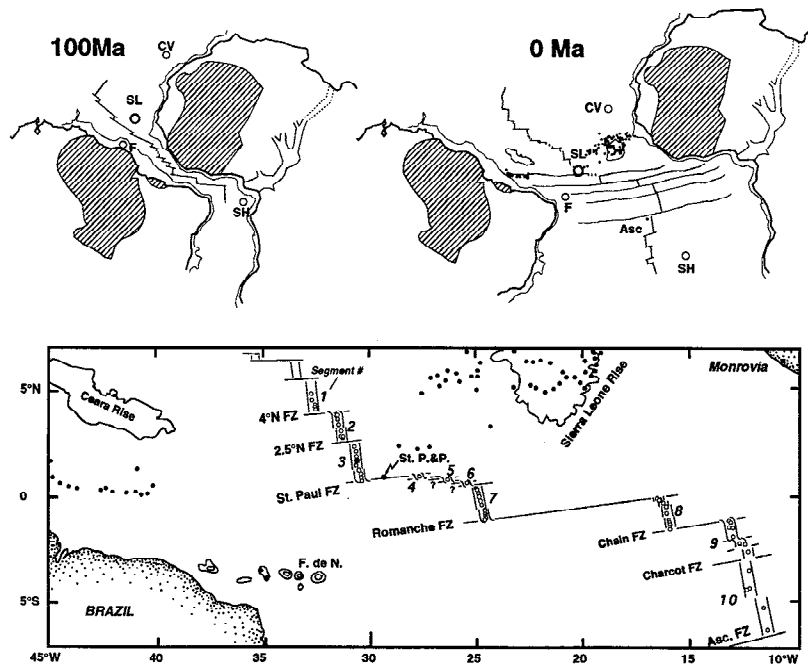

Figure 1. (Bottom) Simplified morphotectonic map of the equatorial Atlantic region showing sample locations along the Mid-Atlantic Ridge axis (open circles). Note position of conjugate aseismic Ceara Rise and Sierra Leone Rise. Solid circles represent seamount locations from *Epp and Smoot* [1989]. (Top) Simplified geological map at 0 and 100 Ma showing position of cold and deep-rooted cratonic lithosphere of Precambrian age (with nuclei reaching Archean age) relative to the Mid-Atlantic Ridge and the equatorial fracture zones. Hotspots: CV, Cape Verde; SL, Sierra Leone; F, Fernando de Noronha; Asc, Ascension; and SH, St. Helena. St. P.&P., St. Peter and Paul's islets. Cretaceous rift east of the West African Precambrian cratons is taken from *Fairhead and Green* [1989]. Adapted from *Schilling et al.* [1994].

Table 1. Major Element Concentrations in Basalt Glasses From the Equatorial Mid-Atlantic Ridge

Sample	Latitude °N	Longitude °W	Depth	Segment	SiO$_2$	Al$_2$O$_3$	FeO^T	MgO	CaO	Na$_2$O	K$_2$O	TiO$_2$	MnO	P$_2$O$_5$	Total	Cr*
RC2806 55D-2g	4.907	32.688	3530	1	50.55	15.31	9.20	8.29	11.73	2.87	0.17	1.36	0.18	0.10	99.76	280
RC2806 55D-3g	4.907	32.688	3530	1	51.16	15.36	9.35	8.16	11.54	2.81	0.16	1.38	0.17	0.11	100.20	265
RC2806 56D-3g	4.613	32.665	3417	1	50.79	15.43	9.45	8.59	12.06	2.60	0.05	1.20	0.18	0.08	100.43	321
RC2806 57D-1g	4.372	32.578	3885	1	50.62	14.57	9.39	8.45	11.10	2.73	0.12	1.46	0.19	0.12	98.75	287
RC2806 57D-2g	4.372	32.578	3885	1	50.89	15.11	9.50	8.02	11.22	2.84	0.13	1.50	0.19	0.10	99.50	
RC2806 58D-1g	4.290	32.579	4040	1	51.03	15.34	9.58	8.21	11.67	2.53	0.10	1.39	0.17	0.10	100.12	328
RC2806 59D-1g	4.195	32.578	4120	1	50.92	14.26	9.77	8.31	10.94	2.72	0.11	1.54	0.17	0.12	98.86	300
RC2806 59D-7g	4.195	32.578	4120	1	51.09	14.71	9.84	7.75	11.02	2.81	0.12	1.57	0.17	0.12	99.20	
4°N Fracture Zone (length† = 120 km; age discontinuity ~7 m.y.)																
RC2806 53D-4g	3.967	31.550	4430	2	51.41	14.00	10.28	7.26	11.33	2.64	0.13	1.62	0.21	0.13	99.01	220
RC2806 53D-6g	3.967	31.550	4430	2	51.42	13.93	10.69	7.09	11.30	2.67	0.14	1.66	0.19	0.13	99.22	
RC2806 54D-1g	3.934	31.556	4471	2	51.77	14.38	10.31	7.58	11.90	2.60	0.10	1.45	0.18	0.10	100.37	291
RC2806 51D-1g	3.919	31.548	4523	2	49.15	16.52	8.70	9.10	11.59	2.50	0.06	0.88	0.16	0.06	98.72	259
RC2806 50D-1g	3.908	31.516	4130	2	51.55	15.08	9.84	8.26	11.09	2.65	0.12	1.44	0.20	0.10	100.33	296
RC2806 49D-1g	3.701	31.513	3737	2	51.61	14.16	9.56	7.60	11.75	2.62	0.06	1.26	0.19	0.09	98.90	237
RC2806 49D-2g	3.701	31.513	3737	2	51.59	14.22	9.56	7.63	11.81	2.63	0.06	1.28	0.19	0.09	99.06	
RC2806 49D-3g	3.701	31.513	3737	2	51.79	14.43	9.70	7.71	11.82	2.69	0.07	1.29	0.18	0.09	99.77	
RC2806 48D-9g	3.458	31.490	3895	2	51.33	15.15	9.45	8.63	11.59	2.59	0.16	1.33	0.16	0.11	100.50	336
RC2806 47D-1g	3.132	31.364	3815	2	51.67	14.24	11.38	7.16	10.84	2.77	0.15	1.84	0.20	0.13	100.38	203
RC2806 45D-1g	2.870	31.345	3070	2	50.93	14.67	9.07	7.77	11.25	2.73	0.25	1.51	0.16	0.16	98.50	281
RC2806 45D-3g	2.870	31.345	3070	2	50.79	14.68	9.14	7.77	11.23	2.67	0.26	1.53	0.17	0.15	98.39	
RC2806 45D-4g	2.870	31.345	3070	2	51.35	14.91	9.18	7.78	11.25	2.74	0.26	1.55	0.18	0.14	99.34	297
RC2806 44D-1g	2.867	31.268	3513	2	50.57	15.81	9.83	8.62	11.51	2.37	0.10	1.18	0.17	0.08	100.24	463
RC2806 46D-1g	2.811	31.286	3682	2	51.16	14.36	9.11	8.02	12.07	2.27	0.10	1.21	0.18	0.10	98.58	311
RC2806 46D-2g	2.811	31.286	3682	2	51.46	14.65	8.88	8.32	12.21	2.27	0.10	1.14	0.17	0.09	99.29	
RC2806 46D-3g	2.811	31.286	3682	2	51.40	14.84	8.92	8.41	12.02	2.31	0.10	1.13	0.17	0.08	99.38	
2.5°N FZ (length = 60 km; age discontinuity ~3.4 m.y.)																
RC2806 43D-5g	2.385	30.768	3674	3	51.41	14.50	8.61	7.52	12.08	2.53	0.35	1.37	0.16	0.15	98.68	335
RC2806 42D-7g	2.176	30.676	3440	3	52.11	14.79	9.04	8.16	10.87	2.72	0.48	1.60	0.15	0.18	100.10	753
RC2806 41D-1g	1.930	30.639	3190	3	51.68	14.22	9.80	6.49	10.79	2.71	0.55	1.76	0.20	0.23	98.43	94
RC2806 41D-2g	1.930	30.639	3190	3	51.81	14.22	9.85	6.50	10.75	2.70	0.54	1.78	0.19	0.21	98.55	
RC2806 41D-3g	1.930	30.639	3190	3	52.06	14.34	9.81	6.57	10.77	2.76	0.55	1.76	0.18	0.20	99.00	
RC2806 41D-4g	1.930	30.639	3190	3	51.99	14.38	9.84	6.55	10.77	2.75	0.55	1.71	0.18	0.21	98.93	
RC2806 40D-3g	1.704	30.640	3515	3	51.05	15.39	8.65	7.49	11.20	2.88	0.88	1.84	0.15	0.26	99.79	321
RC2806 40D-9g	1.704	30.640	3515	3	50.32	15.34	8.74	7.58	11.21	2.99	0.85	1.86	0.17	0.26	99.32	325
RC2806 39D-1g	1.506	30.667	3450	3	51.64	15.33	8.96	7.56	11.83	2.62	0.54	1.64	0.16	0.19	100.47	265
RC2806 38D-1g	1.289	30.535	3690	3	50.28	15.98	9.10	8.95	12.27	2.34	0.15	1.14	0.15	0.09	100.45	388
RC2806 38D-2g	1.289	30.535	3690	3	49.72	15.98	8.93	9.00	12.42	2.39	0.15	1.11	0.18	0.08	99.96	382
RC2806 37D-1g	1.096	30.437	3345	3	50.33	15.54	9.49	8.28	11.77	2.64	0.36	1.41	0.15	0.15	100.12	373
RC2806 37D-2g	1.096	30.437	3345	3	49.36	15.31	9.51	8.54	11.97	2.61	0.35	1.43	0.18	0.13	99.39	
RC2806 36D-1g	0.954	30.416	3285	3	52.15	14.94	9.37	7.86	11.69	2.44	0.27	1.39	0.17	0.13	100.41	239
RC2806 36D-2g	0.954	30.416	3285	3	51.25	14.45	9.40	7.80	11.39	2.54	0.29	1.45	0.17	0.15	98.89	
RC2806 36D-3g	0.954	30.416	3285	3	51.36	14.75	9.40	7.94	11.85	2.53	0.28	1.44	0.17	0.12	99.84	
RC2806 35D-2g	0.789	30.400	3740	3	51.98	14.79	9.69	7.91	11.40	2.58	0.31	1.52	0.17	0.15	100.50	382

Table 1. (continued)

Sample ID	Latitude °N	Longitude °W	Depth	Segment	SiO$_2$	Al$_2$O$_3$	FeO^T	MgO	CaO	Na$_2$O	K$_2$O	TiO$_2$	MnO	P$_2$O$_5$	Total	Cr*
RC2806 35D-4g	0.789	30.400	3740	3	51.16	14.74	9.66	7.98	11.33	2.68	0.30	1.56	0.17	0.15	99.73	315
RC2806 35D-8g	0.789	30.400	3740	3	51.41	14.90	9.69	7.95	11.45	2.33	0.30	1.51	0.18	0.14	99.86	368
W. St. Paul FZ (length = 300km; age discontinuity ~17 m.y.)																
RC2806 34D-1g	1.023	27.702	4530	4	50.59	15.86	9.99	6.54	10.39	3.58	0.66	1.81	0.20	0.23	99.85	172
RC2806 34D-2g	1.023	27.702	4530	4	49.87	15.70	9.75	6.41	10.58	3.50	0.64	1.85	0.19	0.24	98.73	344
RC2806 33D-1g	0.986	27.691	4470	4	52.18	15.73	9.72	6.07	9.75	3.74	0.66	1.95	0.15	0.27	100.22	161
Intra-transform (length = 143 km; age discontinuity ~8 m.y.)																
RC2806 32D-1g	0.821	26.352	4665	5	51.63	15.45	10.11	6.90	10.31	3.54	0.15	1.77	0.18	0.16	100.20	300
Intra-transform (length = 94km; age discontinuity ~5my)																
RC2806 30D-1g	0.669	25.459	4578	6	50.37	14.93	10.22	7.08	11.19	3.41	0.08	1.59	0.22	0.15	99.24	
RC2806 31D-1g	0.654	25.455	4414	6	52.26	15.08	10.38	6.52	9.82	3.96	0.16	1.91	0.20	0.19	100.48	204
RC2806 31D-2g	0.654	25.455	4414	6	51.60	14.91	9.83	6.56	10.14	3.89	0.15	1.88	0.21	0.19	99.36	
RC2806 31D-3g	0.654	25.455	4414	6	51.65	14.83	10.14	6.52	10.17	3.97	0.17	1.91	0.21	0.21	99.78	195
Intra-transform (length = 47 km; age discontinuity ~2.7 m.y.)																
RC2806 29D-1g	0.481	25.028	3975	7	51.88	15.16	9.53	7.42	11.10	3.18	0.15	1.67	0.17	0.13	100.39	
RC2806 29D-2g	0.481	25.028	3975	7	52.09	15.10	9.49	7.37	11.05	3.14	0.14	1.67	0.18	0.13	100.36	
RC2806 29D-3g	0.481	25.028	3975	7	52.17	15.16	9.35	7.33	11.08	3.11	0.16	1.66	0.18	0.14	100.34	286
RC2806 28D-1ag	0.365	24.973	3989	7	51.72	15.14	9.46	7.58	11.18	3.12	0.13	1.55	0.17	0.11	100.16	359
RC2806 27D-4g	0.183	24.909	3944	7	52.17	14.63	10.02	6.85	10.88	3.20	0.16	1.87	0.19	0.16	100.13	203
RC2806 27D-7g	0.183	24.909	3944	7	52.17	14.74	10.05	6.92	10.86	3.20	0.16	1.87	0.18	0.16	100.31	
RC2806 26D-1g	0.037	24.872	3950	7	52.08	14.86	10.23	6.97	10.52	3.28	0.20	1.89	0.19	0.18	100.40	180
RC2806 26D-6g	0.037	24.872	3950	7	51.43	14.56	10.18	6.93	10.51	3.30	0.21	1.95	0.18	0.17	99.42	
RC2806 25D-1g	-0.151	24.813	3845	7	51.40	14.04	10.25	6.67	10.71	3.25	0.18	2.03	0.19	0.19	98.91	
RC2806 25D-2g	-0.151	24.813	3845	7	51.11	14.20	10.06	6.79	10.70	3.21	0.17	1.98	0.19	0.19	98.60	231
RC2806 25D-3g	-0.151	24.813	3845	7	51.53	14.50	9.73	7.32	10.86	3.13	0.15	1.75	0.18	0.15	99.30	
RC2806 24D-1g	-0.333	24.755	2957	7	52.31	14.61	10.09	6.84	10.82	3.45	0.22	1.84	0.19	0.13	100.50	217
RC2806 24D-4g	-0.333	24.755	2957	7	51.56	14.62	9.32	7.35	11.54	3.37	0.13	1.49	0.19	0.12	99.69	200
RC2806 23D-1g	-0.572	24.612	3362	7	51.60	15.28	9.25	8.07	11.09	3.09	0.13	1.53	0.17	0.14	100.35	259
RC2806 23D-2g	-0.572	24.612	3362	7	52.17	14.60	9.39	7.84	11.75	2.86	0.11	1.42	0.17	0.10	100.41	
RC2806 22D-1g	-0.791	24.611	3895	7	51.28	13.99	10.89	6.67	11.00	3.29	0.16	2.01	0.21	0.15	99.65	
RC2806 22D-2g	-0.791	24.611	3895	7	50.95	14.35	9.92	7.20	11.32	2.96	0.14	1.87	0.20	0.14	99.05	
RC2806 22D-4g	-0.791	24.611	3895	7	52.04	14.74	9.90	7.18	10.94	3.25	0.16	1.73	0.19	0.13	100.26	219
RC2806 21D-1g	-0.892	24.578	4275	7	50.82	15.40	9.63	8.31	11.12	2.81	0.11	1.47	0.18	0.11	99.96	245
RC2806 19D-1g	-1.013	24.604	3690	7	51.41	15.04	9.83	7.56	11.19	3.01	0.13	1.68	0.18	0.12	100.15	315
Romanche FZ (length = 920 km; age discontinuity ~50 m.y.)																
RC2806 18D-1g	-0.044	16.467	3836	8	52.30	15.90	7.52	7.04	9.76	3.73	0.52	1.54	0.15	0.25	98.71	252
RC2806 18D-2g	-0.044	16.467	3836	8	52.22	15.83	7.54	6.99	9.67	3.75	0.52	1.58	0.15	0.26	98.51	257
RC2806 18D-3g	-0.044	16.467	3836	8	52.45	15.98	7.70	7.12	9.68	3.88	0.53	1.57	0.14	0.24	99.29	
RC2806 7D-1g	-0.136	16.429	4000	8	50.25	15.88	8.70	6.71	11.21	3.41	0.98	2.03	0.14	0.34	99.65	336
RC2806 7D-3g	-0.136	16.429	4000	8	50.17	15.64	8.75	6.78	11.24	3.38	0.97	2.00	0.14	0.13	99.20	
RC2806 7D-4g	-0.136	16.429	4000	8	50.24	15.56	8.79	6.66	11.19	3.38	1.01	2.03	0.14	0.14	99.14	
RC2806 16D-1g	-0.270	16.235	4095	8	51.47	15.96	10.39	7.53	9.69	3.04	0.05	1.18	0.17	0.06	99.54	214
RC2806 16D-10g	-0.270	16.235	4095	8	51.12	15.26	8.94	8.04	11.00	3.22	0.28	1.58	0.17	0.16	99.77	326
RC2806 16D-2g	-0.270	16.235	4095	8	51.35	15.14	8.92	8.81	10.97	3.06	0.28	1.43	0.16	0.16	100.28	

Table 1. (continued)

Sample ID	Latitude °N	Longitude °W	Depth	Segment	SiO$_2$	Al$_2$O$_3$	FeO^T	MgO	CaO	Na$_2$O	K$_2$O	TiO$_2$	MnO	P$_2$O$_5$	Total	Cr*
RC2806 16D-4g	-0.270	16.235	4095	8	49.32	16.31	10.69	9.21	10.62	2.79	0.09	0.90	0.20	0.07	100.20	
RC2806 16D-5g	-0.270	16.235	4095	8	51.69	15.71	10.72	7.71	9.61	3.04	0.11	1.14	0.18	0.06	99.97	
RC2806 16D-6g	-0.270	16.235	4095	8	49.42	16.33	10.66	9.05	10.69	2.77	0.09	0.91	0.19	0.07	100.18	
RC2806 16D-8g	-0.270	16.235	4095	8	51.92	15.12	9.05	8.17	10.72	3.21	0.29	1.56	0.15	0.17	100.36	269
RC2806 8D-1g	-0.405	16.089	4220	8	51.12	15.27	9.32	7.87	10.83	3.20	0.27	1.57	0.18	0.21	99.84	
RC2806 8D-2g	-0.405	16.089	4220	8	51.88	14.31	9.84	6.98	11.09	3.05	0.23	1.80	0.19	0.15	99.52	
RC2806 9D-3g	-0.742	16.077	4305	8	51.94	13.93	10.59	6.48	10.66	3.22	0.24	1.97	0.21	0.18	99.42	164
RC2806 9D-4g	-0.742	16.077	4305	8	52.06	13.93	10.54	6.51	10.60	3.17	0.24	1.92	0.19	0.18	99.34	
RC2806 10D-4g	-1.062	15.976	4000	8	51.55	14.63	9.71	7.86	10.96	3.02	0.16	1.66	0.17	0.13	99.85	
RC2806 10D-5g	-1.062	15.976	4000	8	51.56	14.80	9.69	7.67	10.98	3.02	0.18	1.65	0.17	0.08	99.80	258
RC2806 10D-6g	-1.062	15.976	4000	8	51.47	15.10	9.40	7.83	10.99	3.05	0.17	1.62	0.17	0.14	99.94	
RC2806 10D-9g	-1.062	15.976	4000	8	51.50	14.71	9.77	7.87	10.92	2.97	0.16	1.65	0.18	0.09	99.82	195
RC2806 14D-2g	-1.159	15.938	3930	8	51.12	14.45	10.60	6.85	10.80	3.16	0.22	1.96	0.18	0.16	99.50	
RC2806 14D-3g	-1.159	15.938	3930	8	51.92	14.41	10.84	6.91	10.64	3.13	0.23	1.94	0.18	0.17	100.37	
RC2806 14D-4g	-1.159	15.938	3930	8	51.74	14.36	10.82	6.93	10.60	3.21	0.23	1.94	0.20	0.17	100.20	
RC2806 14D-7g	-1.159	15.938	3930	8	51.63	14.97	9.78	7.45	11.04	3.07	0.19	1.61	0.18	0.15	100.07	250
RC2806 14D-8g	-1.159	15.938	3930	8	51.58	15.03	9.66	8.01	10.96	3.00	0.21	1.54	0.18	0.14	100.31	
RC2806 11D-1g	-1.261	15.920	4355	8	50.51	15.73	8.29	9.06	12.04	2.55	0.11	1.09	0.15	0.08	99.61	390
RC2806 11D-3g	-1.261	15.920	4355	8	50.76	15.50	8.39	9.20	11.96	2.51	0.12	1.10	0.17	0.08	99.79	
RC2806 11D-4g	-1.261	15.920	4355	8	51.11	15.61	8.44	9.17	12.02	2.51	0.11	1.09	0.17	0.38	100.61	
RC2806 11D-6g	-1.261	15.920	4355	8	51.13	15.70	8.53	9.13	12.03	2.49	0.12	1.10	0.15	0.08	100.46	
RC2806 13D-2g	-1.365	15.919	4580	8	51.63	15.15	9.60	8.13	11.18	2.91	0.16	1.45	0.17	0.13	100.51	
RC2806 13D-3g	-1.365	15.919	4580	8	51.52	15.18	9.40	8.38	11.22	2.84	0.15	1.43	0.17	0.13	100.42	319
RC2806 13D-4g	-1.365	15.919	4580	8	51.52	15.34	9.45	8.34	11.20	2.86	0.15	1.43	0.17	0.12	100.58	
RC2806 12D-1g	-1.536	15.888	4376	8	50.76	15.63	9.15	8.04	11.13	3.13	0.17	1.52	0.17	0.14	99.84	290
RC2806 12D-2g	-1.536	15.888	4376	8	51.47	15.15	9.47	8.10	10.82	3.04	0.20	1.51	0.17	0.13	100.06	
RC2806 12D-3g	-1.536	15.888	4376	8	51.13	15.52	9.23	8.09	10.99	3.12	0.18	1.50	0.17	0.13	100.06	
RC2806 12D-4g	-1.536	15.888	4376	8	51.55	15.01	9.67	8.23	10.69	2.97	0.20	1.56	0.18	0.13	100.19	
RC2806 12D-5g	-1.536	15.888	4376	8	51.72	15.18	9.61	8.08	10.90	3.00	0.19	1.54	0.18	0.13	100.53	
RC2806 12D-6g	-1.536	15.888	4376	8	51.26	15.53	9.31	8.07	11.19	3.08	0.18	1.52	0.17	0.13	100.44	
RC2806 12D-7g	-1.536	15.888	4376	8	51.72	15.13	9.55	8.02	10.85	3.01	0.21	1.55	0.18	0.13	100.35	
Chain FZ (length = 315 km; age discontinuity ~17 m.y.)																
RC2806 6D-1g	-1.051	13.112	4175	9	51.57	14.66	9.56	7.49	10.82	3.23	0.16	1.54	0.18	0.14	99.35	203
RC2806 6D-2g	-1.051	13.112	4175	9	51.25	14.68	9.70	7.79	10.95	2.97	0.13	1.49	0.19	0.13	99.28	
RC2806 6D-3g	-1.051	13.112	4175	9	51.33	14.83	9.77	7.75	11.01	2.98	0.13	1.46	0.15	0.11	99.52	
RC2806 5D-1g	-1.162	13.068	3975	9	51.47	15.14	9.77	7.51	11.28	2.95	0.20	1.65	0.17	0.15	100.29	289
RC2806 5D-2g	-1.162	13.068	3975	9	51.43	14.86	9.92	7.56	11.31	2.94	0.21	1.64	0.18	0.14	100.19	282
RC2806 5D-3g	-1.162	13.068	3975	9	51.53	14.87	9.87	7.57	11.28	2.91	0.21	1.65	0.19	0.34	100.42	
RC2806 5D-4g	-1.162	13.068	3975	9	51.51	14.75	9.96	7.53	11.26	2.92	0.21	1.67	0.18	0.19	100.18	
EN061 1D-1g	-1.407	13.175	2600	9	51.08	16.09	8.61	8.58	11.51	2.87	0.11	1.21	0.18	0.27	100.51	325
RC2806 4D-1g	-1.409	13.007	3950	9	48.80	15.24	9.74	7.46	12.11	2.95	0.88	1.85	0.16	0.14	99.33	331
RC2806 4D-2g	-1.409	13.007	3950	9	48.82	15.34	9.76	7.53	12.02	2.96	0.88	1.83	0.15	0.11	99.44	
RC2806 4D-3g	-1.409	13.007	3950	9	48.62	15.46	9.62	7.40	12.12	3.00	0.87	1.84	0.18	0.24	99.35	297
RC2806 3D-1g	-1.843	12.955	3800	9	51.46	15.24	9.50	7.96	11.18	2.86	0.28	1.59	0.18	0.24	100.49	

Table 1. (continued)

Sample ID	Latitude °N	Longitude °W	Depth	Segment	SiO$_2$	Al$_2$O$_3$	FeO^T	MgO	CaO	Na$_2$O	K$_2$O	TiO$_2$	MnO	P$_2$O$_5$	Total	Cr*
RC2806 3D-2g	-1.843	12.955	3800	9	51.28	15.38	9.34	7.86	11.18	2.92	0.29	1.53	0.16	0.15	100.09	263
RC2806 3D-3g	-1.843	12.955	3800	9	51.41	15.27	9.60	7.90	11.17	2.90	0.29	1.56	0.17	0.25	100.52	384
RC2806 2D-1g	-2.178	12.635	3857	9	51.21	15.82	8.50	8.95	12.00	2.55	0.07	1.17	0.15	0.09	100.51	
RC2806 2D-2g	-2.178	12.635	3857	9	51.23	15.56	8.67	8.79	12.03	2.53	0.07	1.23	0.14	0.15	100.40	
RC2806 2D-3g	-2.178	12.635	3857	9	51.35	15.73	8.54	8.91	12.08	2.57	0.06	1.18	0.16	0.14	100.72	
EN061 2D-1g	-2.238	12.397	3885	9	50.34	16.13	8.93	9.01	11.74	2.40	0.04	1.21	0.18	0.36	100.34	367
RC2806 1D-1g	-2.540	12.233	3740	9	50.78	15.27	9.32	8.69	12.53	2.36	0.04	1.14	0.16	0.07	100.36	372
RC2806 1D-2g	-2.540	12.233	3740	9	50.88	15.06	9.34	8.75	12.43	2.29	0.03	1.13	0.17	0.09	100.17	
RC2806 1D-3g	-2.540	12.233	3740	9	50.92	15.06	9.44	8.79	12.43	2.28	0.03	1.11	0.18	0.10	100.34	
Charcot FZ (length = 32 km; age discontinuity ~1.7 m.y.)																
EN061 3D-1	-3.433	12.225	3045	10	51.04	15.66	8.81	8.76	11.90	2.43	0.06	1.19	0.18	0.27	100.30	330
EN061 4D-1g	-4.272	12.198	2300	10	50.97	15.13	9.80	8.11	11.48	2.66	0.08	1.46	0.21	0.30	100.20	287
EN061 5D-1Ag	-5.185	11.517	3300	10	51.08	14.67	10.36	8.40	11.12	2.37	0.12	1.34	0.21	0.32	99.99	254
EN061 6D-1Cg	-6.310	11.322	3218	10	51.05	15.74	9.34	8.94	10.76	2.54	0.10	1.09	0.19	0.27	100.02	342

The microprobe analyses were performed on a Cameca Camebax SX50 three-spectrometer electron probe microanalyzer, using a 10 μm defocused beam, 15 kV acceleration voltage, 10 nA beam current. Ten to 15 points were analyzed on at least three glass chips per sample and averaged. Matrix corrections were performed on line by the "P&P", $\phi(\rho,z)$ method [Pouchou and Pichoir, 1987]. For additional details of the method contact A. Davis.
* Cr concentration (ppm) by Instrumental Neutron Activation Analysis.
† Transform fault length.

research vessel R/V *Conrad.* In a previous paper we have reported on the Nd, Sr, and Pb isotope and La/Sm variations along the MAR provided by these basalt glasses and discussed the implications of these results for the nature and length scale of mantle heterogeneities and the dynamics of plume dispersion in the region [*Schilling et al.*, 1994]. Here we report on the major element composition of these basalt glasses and focus on the implications petrologic variations have on the thermal structure of the upper mantle, melting regime, and magma budget.

Sampling

During the 1987 cruise, fresh glassy pillow basalts were recovered at 55 of the 59 dredge stations spaced at 15-20 km intervals along the axis of the MAR (Figure 1). We followed the volcanically active zone within the well-developed rift valley using the multibeam echosounder Sea Beam system, Global Positioning System navigation, a previous GLORIA side scan survey [*Parson and Searle*, 1986], existing General Bathymetric Chart of the Oceans maps, and an unpublished map provided by M.V. Thomas and R. Searle (personal communication, 1987). In transit along the poorly charted 600-km-long, 100-km-wide St. Paul fracture zone, we located two other, short (~20 km), deep (4-5 km), pull-apart basins, arranged in en echelon pattern. The recovery of fresh, essentially undegassed, volcanic glasses from these two pull-apart basins suggests recent volcanic activity. The lack of well-developed north-south magnetic anomalies at the equator and the existing tectonic complexity make it impossible to determine whether these two volcanically active relay zones represent the loci of seafloor spreading sustained over long periods of time, or alternatively, sites of ephemeral volcanism, along leaky transform faults [*Van Andel et al.*, 1969; *Thompson and Melson*, 1972], or oscillatory spreading [*Bonatti and Crane*, 1982].

Petrologic Results

Table 1 lists the major element compositions of the basaltic glasses studied. The analyses were performed with a Cameca electron microprobe, model Camebax SX50. The analytical conditions used are given in Table 1. We analyzed at least one basaltic glass from each of the 63 stations shown in Figure 1. Also included in the data set are six stations collected between the Chain and the Ascension FZ during R/V *Endeavor* cruise 061. Local major element variability of the equatorial MAR basalt glasses can be evaluated from those stations where more than one sample has been analyzed (Table 1). The length scale of the variability is 1-2 km, which represents the approximate distance the dredge was dragged on the seafloor at each station. In general, the variability is small, but exceptions to this rule occur at the Chain-east RTI (6D) and at or near the Romanche east-RTI (16D and 18D). At both of these sites, the ridge axis is either curving or highly segmented and displaced en echelon (Figure 1). The nature of the variability at the three anomalous stations is discussed below and by *Schilling et al.* [1994]. We also conducted a more systematic investigation of local variations at the 4°N east-RTI, where four well-mapped seamounts were sampled separately (stations 50D to 54D in Table 1). The basalts from 50D, 52D, and 54D form a uniform group comparable to others from segment 2. In contrast, seamount 51D from the deepest part of the rift is more mafic and K$_2$O and light rare earth element (REE) depleted [*Schilling et al.*, 1994]. In this case the length scale of the variation observed is of the order of 10 km.

On the basis of the CIPW norm classification [*Yoder and Tilley*, 1962], 109 of the 140 basalt glasses studied are olivine normative tholeiites (46 stations), 22 are quartz normative tholeiites (11 stations), and 9 are mildly nepheline normative basalts (4 stations). The olivine and quartz normative tholeiites are randomly distributed along the ridge, without showing any particular correlation with tectonic segmentation. This may not be the case for the nepheline normative basalts. Three of the four occurrences observed are located at or near a RTI (Figure 1). The exception is 4D. Station 6D at the Chain east-RTI contains both olivine and nepheline normative basalts. The olivine normative basalt occurs as glassy pillow basalts, while the nepheline normative basalts are represented by highly vesicular, subangular fragments of subaerial morphologic appearance devoid of glass, despite being dredged at 4000-4350 m below sea level. These rocks may represent ejecta from an uncharted shallow seamount or a sunken island. *Bonatti and Honnorez* [1971], *Bonatti* [1973, 1978], and *Bonatti et al.* [1979] have reported evidence suggesting that large-scale subsidence and uplift occurred along the equatorial Atlantic mega-fracture zones and have repeatedly emphasized the unusual nature of opening in this part of the Atlantic. The subaerial morphologic appearance of some of the volcanic rocks dredged at station 6D may be further proof of such unusually intense subsidence. The nepheline normative basalts from station 7D occur near the Romanche east-RTI along a short ridge segment (Figure 1). Finally, the nepheline normative basalts from station 34D were erupted in the short and profoundly deep pull-apart segment 4 located within the St. Paul FZ, just southeast of St. Peter and Paul islets (Figure 1). These nepheline normative basalts are all light-REE enriched and radiogenic Pb and Sr isotope rich but were apparently derived from two distinct enriched mantle domains [*Schilling et al.*, 1994]. As we will see later, they were also generated under conditions of unusually small degrees of partial melting for MORB.

In the triangular Fe-Mg-Na diagram (Figure 2), our dredged basalts indeed confirm the Na-rich character of MORBs in the equatorial Atlantic previously suggested on the basis of meager

sampling [*Dmitriev et al.*, 1979; *Melson and O'Hearn*, 1979]. The equatorial MORB fractionation trend shows limited Fe/Mg enrichment relative to that found along the MAR transect over the Iceland and Azores platforms. The trend of Na enrichment overlaps that of the Azores province, but the similarity ends there. In comparison to MORBs from the Azores province, MORBs from the equatorial Atlantic are generally much richer in SiO_2 (mostly 50 - 52.5%, mean 51.24% ± 0.73, 1 standard deviation) [*Schilling et al.*, 1983]. The equatorial MORBs are similar to those found on the highly fragmented Southwest Indian ridge (SWIR) [*Le Roex et al.*, 1989], in the Australian-Antarctic discordance (AAD) [*Klein et al.*, 1991] and at the Cayman Trough [*Thompson et al.*, 1980]. All of these ridge segments are unusually deep. Their MORB compositions lie at the high end of the global correlation of Na, Fe, and Si with ridge elevation revealed by *Klein and Langmuir* [1987] (subsequently referred to as K&L'87). The compositional similarity of the equatorial Atlantic MORB glasses to those from these deep segments is also evident in the covariation of $CaO/CaO+Na_2O$ with Mg number (Mg #) (Figure 3). Compared to these other deep mid-ocean ridge (MOR) segments, the large variation in $CaO/CaO+Na_2O$ for the equatorial MAR basalt glasses occurs over a narrow range of fairly high Mg # (Figure 3). The range overlaps the compositional field occupied by MORB from the SWIR. *Schouten et al.* [1987] have suggested that in such cases the $CaO/CaO+Na_2O$ ratio is a good proxy for estimating the mean degrees of partial melting beneath the MOR system, since such lavas are not likely to have suffered extensive fractional crystallization, at least not at shallow depth. Thus to a first-order approximation, the bulk compositions of the equatorial MORBs suggest that they were generated by relatively small mean degrees of partial melting at shallow mantle depth (low mean pressure). These results fully confirm *Dmitriev et al.'s* [1979] original observations on the petrogenesis of equatorial MORBs based on a more limited sampling.

Along-Ridge Spatial Variations

Surprisingly, the equatorial Atlantic MORB glasses display very systematic long-wavelength spatial trends in some of the major elements when plotted as a function of cumulative distance along the MAR axis from 5°N (Figure 4). These two-dimensional profiles ignore the major transform fault offsets which divide the MAR axis into 10 first-order segments (Figure 1). Despite this intense segmentation, the long-wavelength major element profiles are remarkably simple. For example, the Na_2O profile is characterized by a relatively constant level over segments 1 to 3, a major discontinuity at the St. Paul FZ, and a 600-km-long negative gradient over segments 4 to 10. Overall, the Na_2O content ranges from a high of 4% over the very short and deepest segments 4 to 6 close to St. Peter and Paul's Rocks, to about 2.4% along segment 10. The long Na_2O gradient is continuous and cuts across the major transform fault offsets without any apparent inflection or change of slope. This observation is even more surprising given the length of the transform faults between segment 4 to 10 (approximately 300 km for both the Chain and the St. Paul FZ and 900 km for the Romanche FZ). The concentration profiles for MgO, CaO, Mg #, $CaO/CaO+Na_2O$, Cr/Cr+Al are also very regular and show a pattern which mirrors that of the Na_2O profile. On the other hand, the pattern of spatial variation for FeO and Al_2O_3 is more diffuse, while that of SiO_2 and TiO_2 is essentially random or nonexistent. Along-ridge major element patterns are best
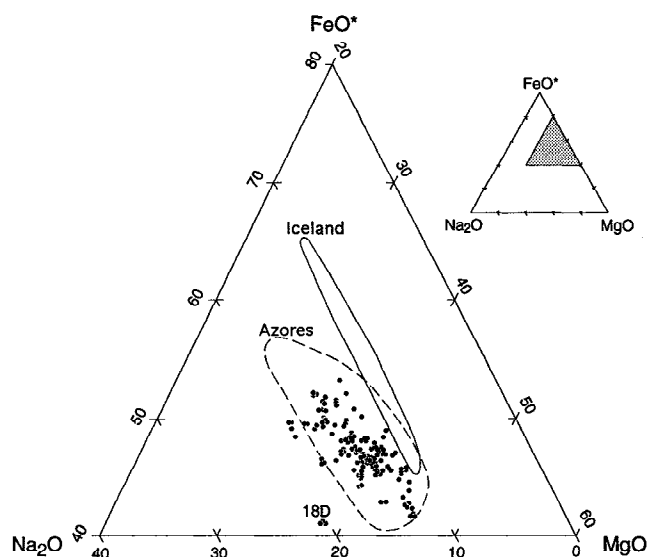

Figure 2. FeO-MgO-Na_2O triangular diagram of MORB glasses from the equatorial MAR. The fields occupied by MORB glasses from the MAR [*Sigurdsson*, 1981] over the Iceland province (solid line) and Azores province (dashed line) are shown for comparison.
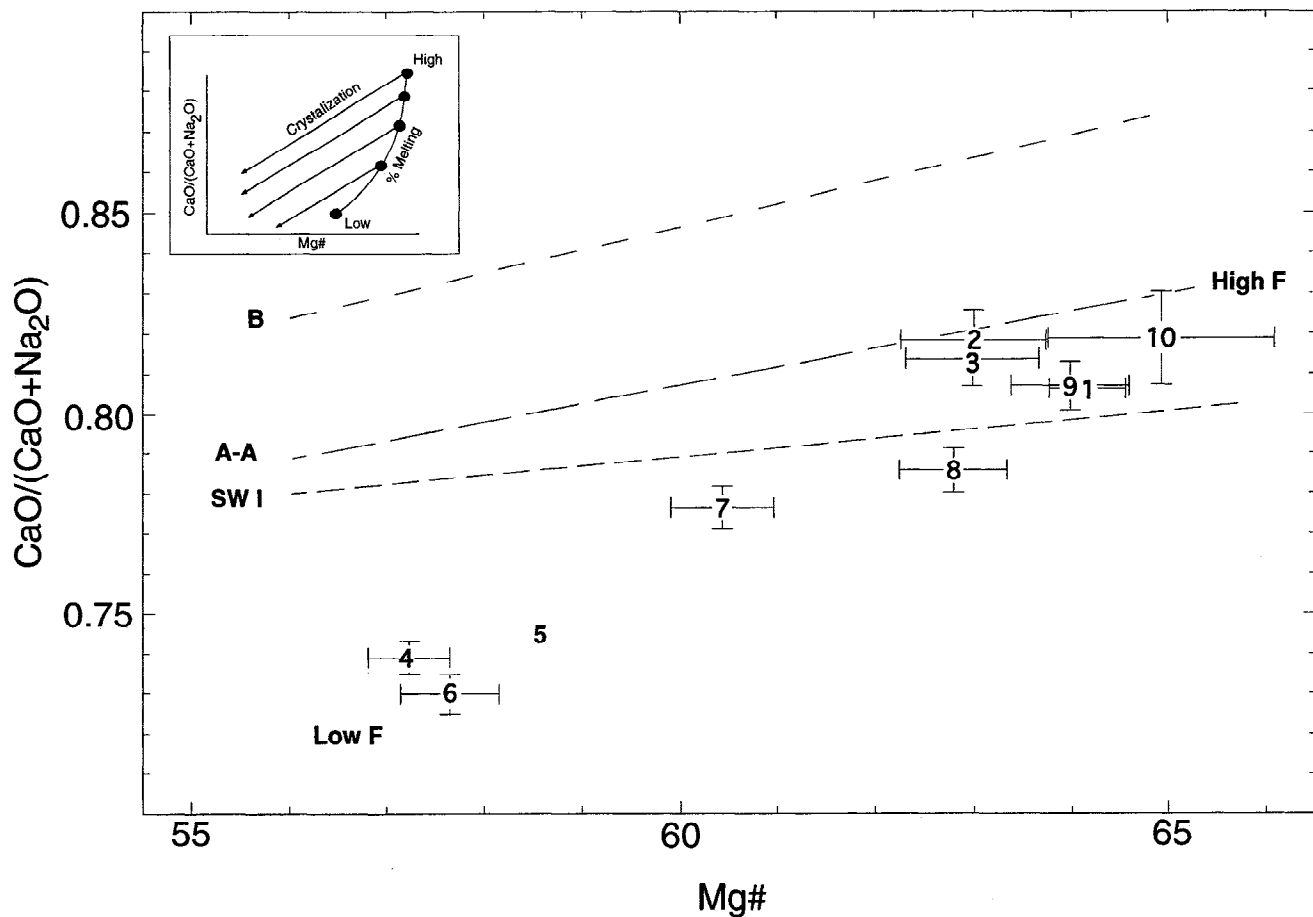
Figure 3. CaO/(CaO + Na$_2$O) wt % ratio versus Mg number in equatorial MORB glasses, averaged per ridge segments 1 to 10 (see Figure 1 for segment locations). Error bars represent 1 standard deviation from the mean. For comparison, mean trends observed in MORBs from the American-Antarctic Ridge (A-A), Southwest Indian Ridge (SWI) and Bouvet (1°-5°E) region and overlapping Southern Mid-Atlantic Ridge (51-55°S) (B) are shown as dashed lines. Adapted from *Schouten et al.* [1987]. An atomic Fe^{3+}/Fe^{2+} + Fe^{3+}= 0.14 was assumed for calculating the Mg numbers.

revealed by averaging the values on a segment by segment basis (Figure 4).

Taking CaO/CaO+Na$_2$O as a first-order proxy for the mean degree of partial melting, the along-ridge profile of this ratio suggests a relative pattern of variation in the degree of melting. Using this interpretation, the data suggest a gradual decrease in the mean degree of partial melting from segment 9 to a minimum over the short pull-apart ridge segments 4 to 6 located within the St. Paul FZ. A major discontinuity occurs at the northern boundary of this diffuse fracture zone. This first-order interpretation, of course, does not take into account secondary, more local, effects caused by the varying degree of fractional crystallization, which undeniably must have taken place along the entire profile. More quantitative and elaborate parameterizations of along-ridge changes in melting conditions are presented below.

The along-ridge profile for K$_2$O is quite distinct and in marked contrast to that of the major elements (Figure 4). The K$_2$O profile is essentially identical to that of La/Sm. These two geochemical parameters are indicative of the current nature of mantle heterogeneity in incompatible elements present beneath the equatorial Atlantic (Figure 4). A full account of the cause of these heterogeneities and their longer-term origin based on Nd-

Sr-Pb isotopic composition of these basalts is given by *Schilling et al.* [1994].

Finally, a few unusual basalt samples are judged to be outliers based on major element covariation diagrams and the along-ridge petrologic profiles. These outliers include basalts from station 7D, 16D, and 18D, all recovered near the tectonically complex Romanche east-RTI. As noted earlier, basalts from stations 4D and 7D are also nepheline normative. These outliers were also identified in multivariate statistical analysis in major element space based on large Mahalanobis distances [*Mahalanobis*, 1936]. They reflect unusually low mantle temperature and partial melting conditions occasionally associated with RTIs due to cold edge effects and have been discussed at greater length by *Schilling et al.* [1994].

Relations to Morphotectonic Ridge Segmentation

Morphotectonic Parameters

Lin et al. [1990] have demonstrated that ridge segment length and axial depth relief are positively correlated between 28°N and 31°N along the MAR. In the same area they note a negative correlation between the intensity of the mantle Bouguer
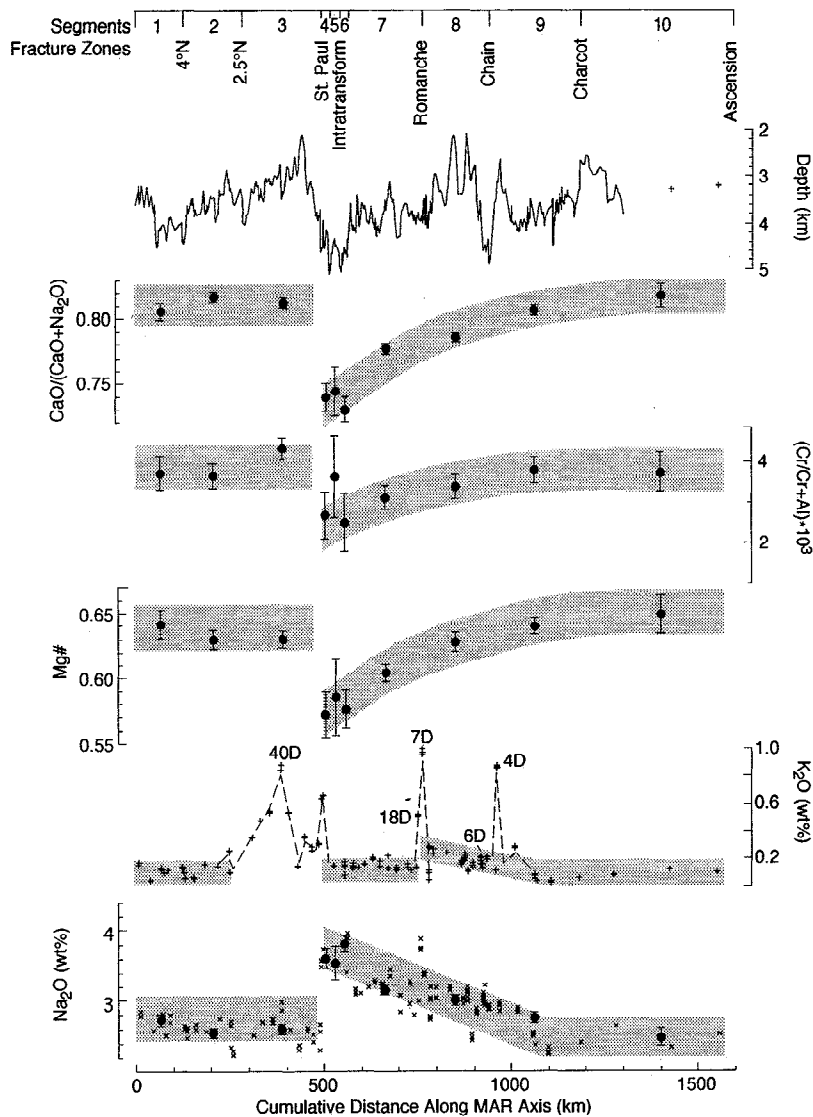
Figure 4. Selected major element contents or ratios in equatorial MORB glasses as a function of cumulative distance along MAR axis from 5°N by adding each segment length one after the other from segment 1 to 10 (see top scale) and excluding transform fault lengths. The chromium number (Cr #) is also for glasses. The data are averaged for each ridge segment (circles) (see Figure 1 for locations). Error bars represent 1 standard deviation from the mean. Entire data set is given in Table 1 and shown only for K_2O and Na_2O (small crosses). The depth profile along the MAR axis (top) is based on Sea Beam data obtained during R/V *Conrad* cruise RC 2806. Note that the depth profile is discontinuous at every fracture zone, whose positions are shown on the top scale.

anomalies and ridge segment length. They have interpreted these observations in terms of mantle upwelling, mode of crustal accretion, and magma budgets as revealed by crustal thickness. Independently, we have investigated some of these relationships in the equatorial Atlantic, in particular, those between transform fault length, mean segment depth, maximum relief per segment, and ridge segment length. The survey is limited to the nine segments between the Charcot FZ and 5°N FZ, which we partially mapped with the Sea Beam system during our sampling cruise aboard the R/V *Conrad*. Our bathymetric data and sampling between the Charcot and Ascension FZ are insufficient to include segment 10 in this exercise.

Some of the empirical relationships among morphotectonic parameters are illustrated in Figure 5. First, we note that there is a fair ($r^2=0.67$) positive correlation between maximum axial

depth relief and segment length (Figure 5a). The slope is 0.0037, compared to 0.02 for the 28°-31°N MAR segment reported by *Lin et al.* [1990] (or 0.016 when additional MAR data between the Hayes to the Oceanographer FZ are included [*Detrick and Needham*, 1992]). The difference between our results and those obtained further north on the MAR may not be significant considering the large uncertainties and preliminary nature of the equatorial data. A higher degree of negative correlation ($r^2=0.82$) is observed between maximum axial relief and mean segment depth based on the dredge stations (Figure 5b). Notably, the shallowest segment 3 also has the second highest relief in the region. This segment is characterized by a major Pb-Nd-Sr isotope and geochemical anomaly, which has been attributed to the influence of the Sierra Leone plume on the MAR [*Schilling et al.*, 1994]. The anomaly is also apparent in the K_2O profile,
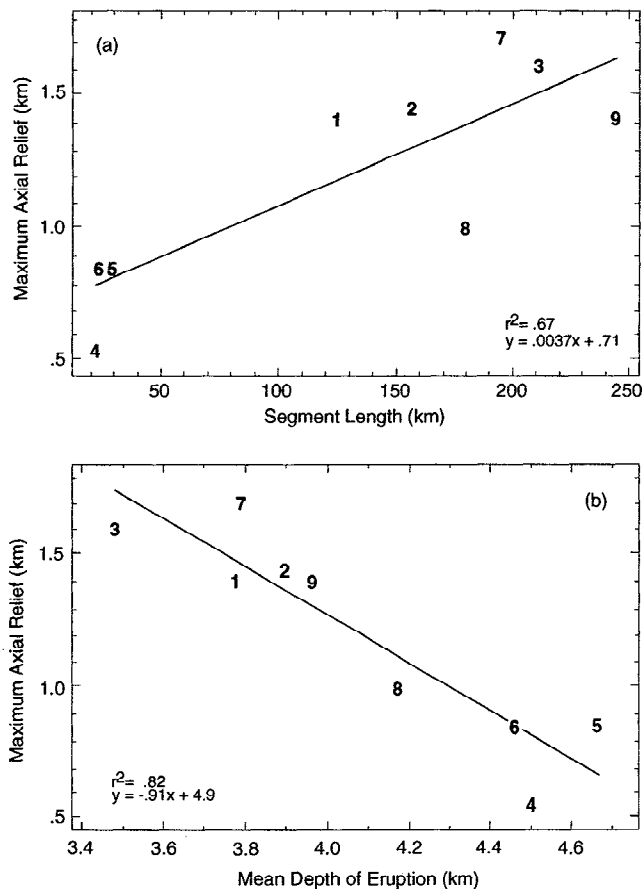
Figure 5. Plot of maximum bathymetric relief along the ridge axis within segments 1 to 10 (Figure 1) against corresponding (top) segment length and (bottom) mean depth of eruption per segment (mean depth of dredge stations per segment). Linear best fit parameters and correlation coefficient are given directly on the two figures.

which mimics that of La/Sm and is quite distinct from that of Na and other major elements (Figure 4). The lowest relief is found in the shortest and deepest segments (pull-aparts) 4 to 6 within the St. Paul FZ. We do not know whether the correlation between these morphotectonic parameters indicates a dichotomy which characterizes only the equatorial Atlantic or reflects an empirical correlation of more general significance for the mid-ocean ridge system. More importantly, none of these morphotectonic parameters correlate with transform fault length in the equatorial Atlantic.

Relationships With Mean Composition per Segment

There is also good and systematic correlation between the major element compositions averaged per segment and the morphotectonic parameters just discussed. For example, a positive correlation between the mean $CaO/CaO+Na_2O$ ratio and segment length (or maximum axial depth relief) is illustrated in Figure 6. The CaO content, Mg #, Cr/Cr+Al, and Ca/Al ratios show the same positive correlation. On the other hand, Na_2O, as well as Na_8, show a negative correlation with segment length (Figure 6). Since ridge length anticorrelates with mean depth per segment, Na_8 positively correlates with average segment depth (Figure 6). Since these parameters are all reasonable proxies for mean degree of melting, $<F>$, it is not surprising to find that the

parameter $<F>$ calculated in the next section also correlates positively with ridge length and maximum axial depth relief and anticorrelates with average segment depth (Figure 7). Again, there is no correlation between transform fault length and the major element parameters or corresponding mean $<F>$.

On the basis of the above correlations one would predict that the mantle Bouguer anomaly in the equatorial Atlantic is likely to show an inverse correlation with calculated $<F>$, crustal thickness, ridge length, and maximum axial depth per segment, and anticorrelate with mean depth per segment, as also observed on the MAR between 25°N and 31°N by Lin et al. [1990]. One would also predict that the long-wavelength equatorial Atlantic profile for the mantle Bouguer anomaly be essentially the mirror image of the calculated $<F>$ profile averaged over segment length as shown in Figure 7. A test of these predictions with actual gravity measurements along the profile will be presented elsewhere.

Test of K&L'87 World-Wide Correlation Model

Klein and Langmuir [1987, 1989] have demonstrated that, after correcting for shallow depth fractional crystallization and averaging over a few hundred kilometers of ridge length, mean Na and Si correlate positively and Fe negatively with mean axial ridge depths. These empirical correlations are dominated by data from ridges shallower than 4 km, since ridge axes deeper than
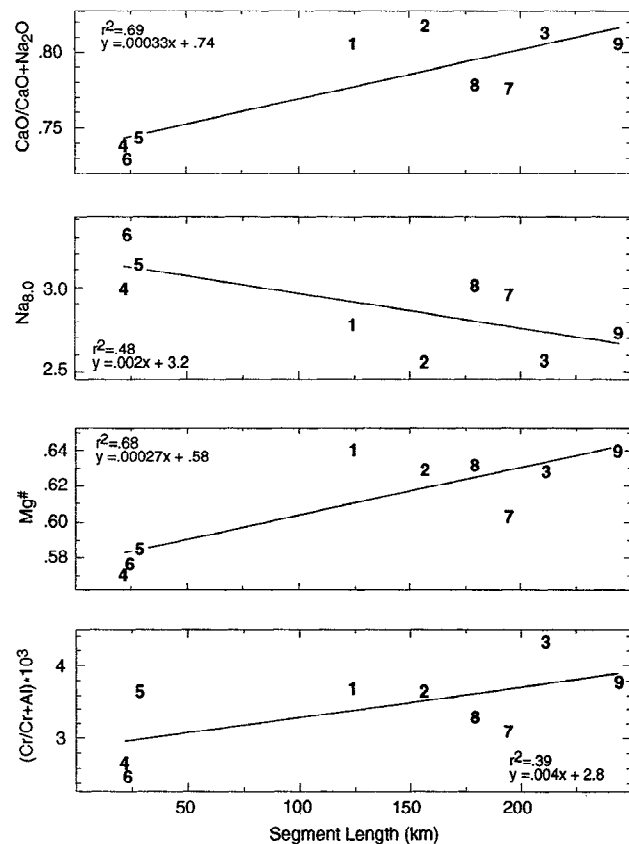
Figure 6. Plots of major and trace element parameters (Cr #) in equatorial MORB glasses averaged per segment against corresponding segment length. See Figure 1 for location of segments 1 to 9. Insufficient sampling prevents reporting a meaningful average for segment 10. Linear best fit parameters and correlation coefficient r^2 are given directly on the plots.
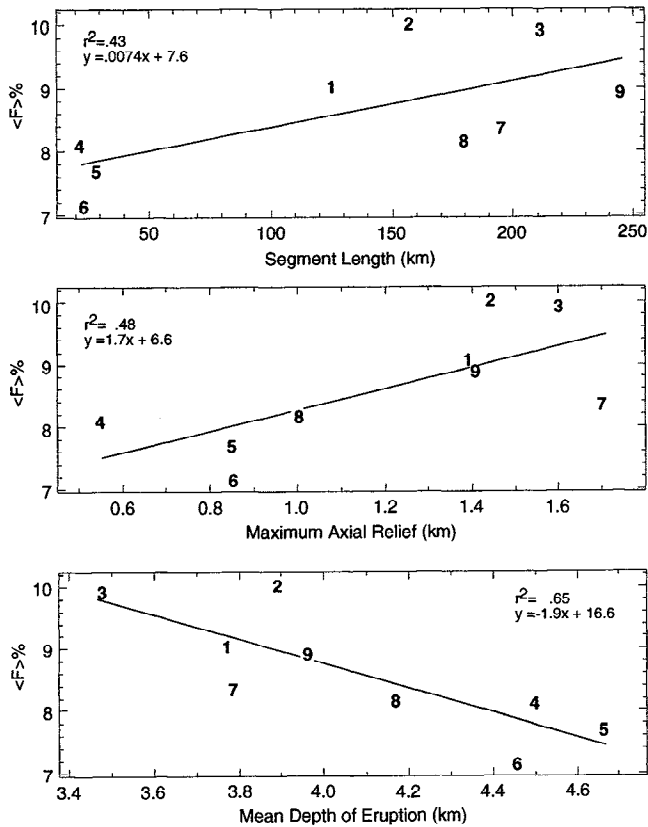
Figure 7. Plots of mean degree of melting ,$<F>$, per ridge segment against corresponding segment length, maximum axial relief, and mean depth of eruption (mean depth of dredge stations) per segment. See Figure 1 for location of segments 1 to 9. Insufficient sampling prevents reporting a meaningful average for segment 10. Linear best fit parameters and correlation coefficient r^2 are given directly on the plots. The parameter $<F>$ is based on the Na_2O content of the MORB glasses and the decompression melting model and methodology of K&L'87. See text and Figure 10 caption for further details on the K&L'87 decompression melting model.

this are rare. However, most of the MORBs dredged along the equatorial MAR are from the 3.5 to 5 km depth range (Figure 4). Therefore our data set provides a good opportunity to test the validity of the K&L'87 empirical relation at these very deep sites within the mid-ocean ridge system.

Following the method of K&L'87, the effect of fractional crystallization at shallow depth was corrected to MgO $\equiv$ 8%, using the actual slopes observed for Na_2O, FeO, and SiO_2 variation relative to MgO in each segment. For the three short pull-apart segments 4 to 6, only one or two samples are available from each segment. We therefore used the best fit slope for the entire MORB population from 3°S to 5°N. A comparison of the best fit slopes calculated for each segment in the equatorial Atlantic and for the global ridge system is shown in Figure 8. Table 2 gives the slope of the best fitting lines and notes which outliers were excluded from the fits. The observed fractionation slope for the overall equatorial Atlantic database is essentially identical to the global one for Na_2O, similar for SiO_2, but significantly different for FeO. As Figure 9a shows, the correlation of Na_8 with depth for the equatorial MORB population is poor but not inconsistent with that of the global

MORB population reported by K&L'87. However, in contrast to the global MORB population, there is no apparent correlation of Fe_8 with depth for the equatorial MAR basalt population (Figure 9b). These results indicate that the negative correlation between Na_8 and Fe_8, which has been noted on a global scale, does not hold up within the equatorial MAR region (Figure 9c).

It has been pointed out that Na_8 and Fe_8 can occasionally be positively correlated at the local scale [*Brodholt and Batiza,* 1989; *Klein and Langmuir,* 1989]. Again, we find no evidence for such a positive correlation between Na_8 and Fe_8 within any of the nine equatorial MAR segments investigated. Thus in the equatorial region there is no justification for projecting each Na_8 or Fe_8 data point onto the global trend, thereby deriving the FeG_8 and SiG_8 parameters of *Klein and Langmuir* [1989]. Such a calculation has been done for equatorial MORBs by *Bonatti et al.* [1993], but we contend that the application of this technique to data in which a positive correlation between Na_8 and Fe_8 is absent in the first place will only force a fictitious correlation.

Niu and Batiza [1993] have recently shown that the so-called local Na_8 versus Fe_8 positive trends are characteristic of slow spreading ridges, whereas the negative global Na_8 versus Fe_8
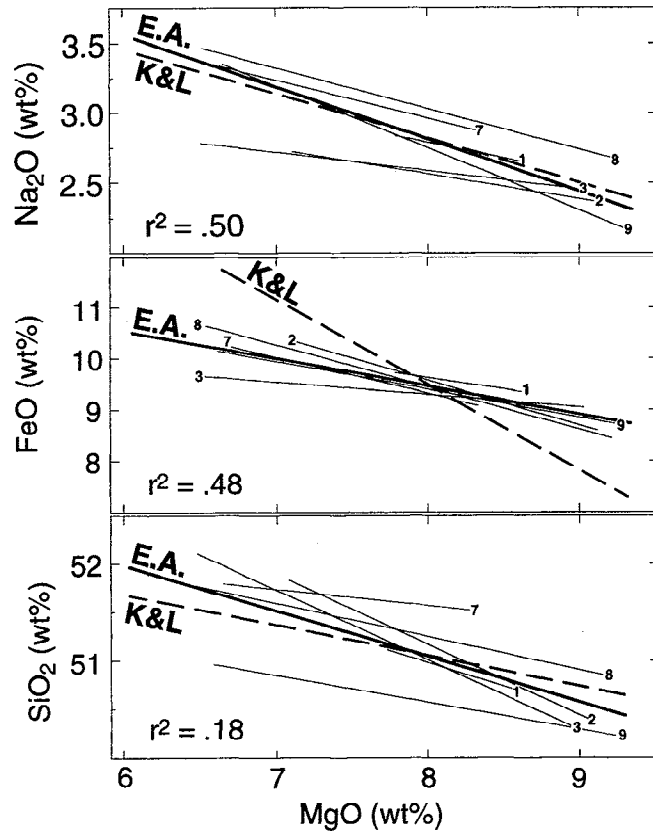

Figure 8. Comparison of the slopes of the best fit lines obtained from scatter diagrams of Na_2O, FeO, and SiO_2 content against MgO content of MORB glasses within ridge segments 1 to 9 (Figure 1), and the entire equatorial Atlantic MORB glass data set from 5°N to 7°S (EA, heavy line). Dashed labeled line (K&L) is the slope used by K&L'87 for filtering low-pressure fractional crystallization and calculating Na_8. Note the good correspondence of EA and K&L slopes for Na_2O and SiO_2 and large discrepancy for FeO. The correlation coefficient r^2 are for the EA lines. Best fit slopes for the ridge segment 1 to 9 are given in Table 2.

Table 2. Slopes and Intercepts for Best Fit Lines Shown in Figure 8

Segment Oxide vs. MgO	1 slope and intercept	2 slope and intercept	3 slope and intercept	4,5,6* slope and intercept	7 slope and intercept	8 slope and intercept	9 and 10 slope and intercept
Na₂O outliers[§]	$-0.218x + 4.53$	$-0.173x + 3.95$	$-0.127x + 3.60$	$-0.345x + 5.60$ 6D-6, 6D-7, 4D, (61)5D	$-0.261x + 5.05$	$-0.286x + 5.31$	$-0.397x + 6.00$ 6D-6, 6D-7, 4D, (61)5D
FeOᵀ outliers	$-0.411x + 12.89$	$-0.863x + 16.46$	$-0.225x + 11.08$	$-0.553x + 13.87$ 7D, 16D, 18D, 6D-6, 6D-7, 4D, (61)5D	$-0.691x + 14.84$	$-0.874x + 16.51$ 7D, 16D, 18D	$-0.693x + 15.04$ 6D-6, 6D-7, 4D, (61)5D
SiO₂ outliers	$-0.496x + 54.96$	$-0.284x + 53.59$ 51D	$-0.718x + 56.76$	$-0.404x + 54.43$ 6D-6, 6D-7, 4D, 51D, (61)5D	$-0.163x + 52.88$	$-0.341x + 53.98$	$-0.441x + 54.81$ 6D-6, 6D-7, 4D, (61)5D
Al₂O₃ outliers	$0.223x + 13.17$	$1.054x + 6.36$	$0.576x + 10.49$	$0.388x + 12.05$ 6D-6, 6D-7, 4D, (61)5D	$0.672x + 9.66$	$0.323x + 12.72$	$0.647x + 9.98$ 6D-6, 6D-7, 4D, (61)5D
CaO outliers	$0.771x + 5.07$	$0.229x + 9.75$	$0.560x + 7.14$	$0.490x + 7.37$ 6D-6, 6D-7, 4D, (61)5D, (61)6D	$0.404x + 8.07$	$0.357x + 8.09$	$0.675x + 5.98$ 6D-6, 6D-7, 4D, (61)5D, (61)6D

* Regional parameters (data of segments 1-9 combined) were used for segments 4, 5, and 6.
§ Outliers not used in regression. Sample number listed are all from cruise RC2806 unless preceded by (61) from cruise EN61.
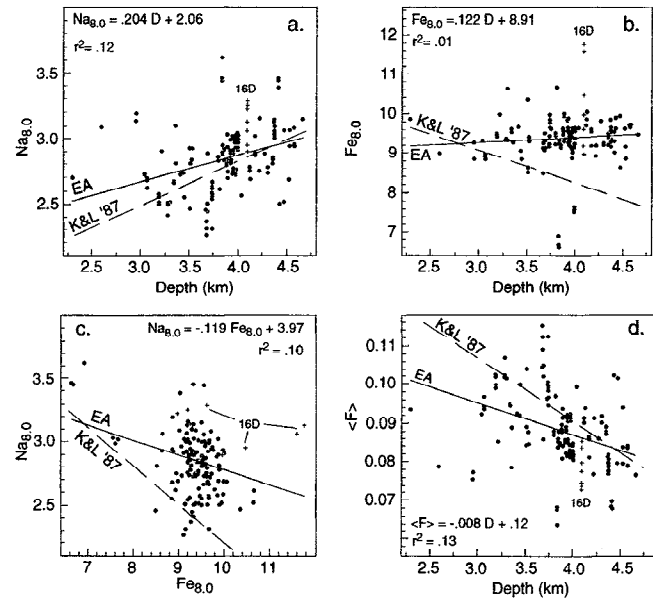
Figure 9. Na₈ versus Fe₈ and Na₈, Fe₈, and mean degree of melting, <F>, plotted against water depth of equatorial MORB glasses. The Na₂O and FeO content at 8% MgO (i.e., Na₈ and Fe₈), used as a filter of low pressure fractional crystallization, were calculated using separate regression lines through segment populations 1 to 9 (Figure 1 and Table 1). The slopes of these lines are given in Table 2. The mean degree of melting is based on Na₂O and K&L'87 petrologic decompression melting model (see caption of Figure 10). Line labeled K&L'87 is the global MORB correlation line of K&L'87. The EA linear best fit line is for the entire equatorial MORB data set from 5°N to 3°S. Note the good correspondence of EA with K&L'87 for Na₈ versus depth, and the lack of correlation for Na₈ versus Fe₈ and Fe₈ versus depth for the EA MORB population.

trend is characteristic of fast spreading ridges. The transition between a negative and positive correlation appears to occur at 36-60 mm/yr full spreading rate. Full spreading rate at the equatorial MAR is approximately 35 mm/yr. Interpreted in light of Niu and Batiza's results, the fact that variations in Na₈ are essentially independent of those in Fe₈ at the equatorial MAR is perhaps not very surprising. Within the 10 individual equatorial MAR segments, we uncovered no local trends in Na₈ versus Fe₈. The only possible exception were basalts recovered at station 16D, where the range of bulk compositions is unusually large (Figure 9c).

Mantle Temperatures and Melting Conditions

There have been several recent attempts to parameterize the major element compositions of MOR basalts in terms of mean properties of melt production. The details of various models differ significantly depending on the assumed melting function, the mode of melt segregation, the assumed flow field, and melt zone geometry. In general, these models yield relationships among melt production parameters such as mantle potential temperature T_o and depth Z_o at which the mantle reaches its melting point during upwelling and decompression, as well as mean pressure of melting <P>, and mean degree of melting <F> [Klein and Langmuir, 1987; McKenzie and Bickle, 1988; Niu and Batiza, 1991; Albarede, 1992; Kinzler and Grove, 1992a, b; Langmuir et al., 1992; Plank and Langmuir, 1992; Kinzler and

Grove, 1993]. These models link major element composition to melt formation parameters on the basis of empirical observations, experimental petrologic data, and various methods of filtering and/or normalizing compositional effects due to fractional crystallization during magma ascent. Although none of the model parameterizations are fully satisfactory and results obtained with each formulation are model dependent, the parameterizations do provide crude but useful constraints on the along-axis, spatial variation in melt production parameters, at least on a relative, if not on an absolute basis.

For simplicity, we apply the model of K&L'87 and *Plank and Langmuir* [1992], which casts variations in melt parameters in terms of variations in Na_8. Figure 10 shows the spatial variation in the mean degree of melting $<F>$, the crustal thickness D_c, the mantle potential temperature T_o, and depth of incipient melting Z_o, calculated on the basis of along-axis changes in Na_8 and assuming a corner flow model. Specifics of the calculation are given in the caption of Figure 10. We note that, over the range of mean degree of partial melting defined by K&L'87's model, these melt production parameters are linearly related within a few percent uncertainty. Thus on a relative basis, Figure 10 shows that the spatial variation in the melt production parameters collapses onto a single profile which mirrors the distribution of Na_2O (Figure 4). Specifically, the curve is characterized by (1) a major negative gradient from the Charcot to the St. Paul FZ, with no apparent inflection or discontinuity at the locations of the major equatorial mega-transform zones, (2) a major discontinuity at the northern boundary of the St. Paul FZ between segments 3

and 4, and (3) further north, a domelike high in initial mantle melting temperature, mean percent melting, crustal thickness, and other melt production parameters. For example, from south to north across the St. Peter and Paul FZ, the potential mantle temperature jumps by about 100°C, the corresponding depth of incipient melting increases by 16 km (45 to 61 km), the mean degree of partial melting rises from 7% to more than 10%, and the crustal thickness nearly doubles (3 to 6 km). The large-scale potential temperature gradient south of this discontinuity is of the order of 0.7°C/km. North of this large discontinuity, the extent of partial melting goes through a broad maximum between 1°-4°N (Figure 10). The high mean percent melting in this vicinity is independently corroborated by the depleted nature of peridotites dredged on the rift mountains in the same equatorial region [*Bonatti et al.*, 1992]. This thermal maximum corresponds also to a major anomaly in Pb isotope ratios, La/Sm, and K_2O variation (Figure 3), which has been attributed to the effect of the Sierra Leone plume on the ridge [*Schilling et al.*, 1994]. The lack of discontinuities in inferred mantle temperature across the mega-transform faults south of the St. Paul FZ suggests that the mantle temperature gradient applies to a broad zone measuring at least 2000 km from east to west in the equatorial Atlantic. This region may correspond to a broad cold zone in the mantle. Also, the deeper and the shorter the ridge segments are, the lower the mantle temperature, mean percent melting and crustal thickness (Figure 7).

The minima in T_o, Z_o, $<F>$ and D_c, depicted in Figure 10, occur over the small relay zones within the St. Paul FZ, which
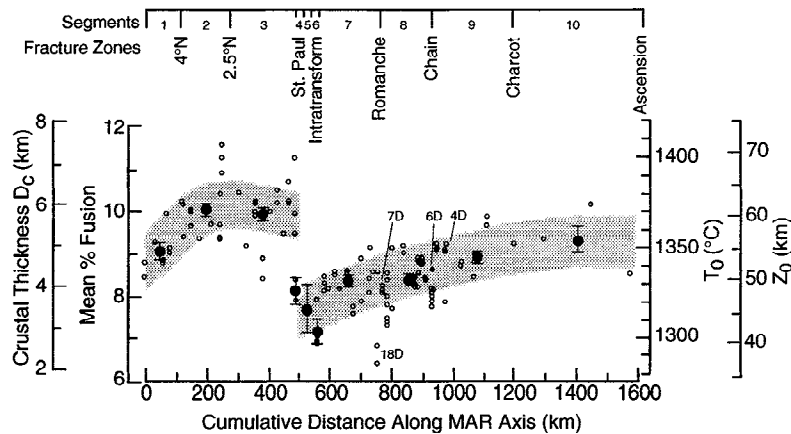

Figure 10. Corresponding mean percent melting, $<F>$, derived from K&L'87 petrologic decompression melting model, using the Na_2O content at MgO = 8% (Na_8) as a filter of low pressure fractional crystallization. The mean degree of melting $<F>$ was obtained by integrating equation (9) in K&L'87 for a corner flow and triangular melting zone model, and by assuming that the accumulated melt concentration $<C_L>$ (*F*) is given by equation (14) of *Shaw* [1970] for continuous fractional melting, thus giving: $<C_L> = (2\ C_o/F_o^2)\{F_o+(D_o/D_o+1)\ ((1-F_o)^{(D+1)/D} -1)\}$, where $<C_L>$ = mean concentration in the accumulated melt (= Na_8 in glass), $C_o = Na_2O$ concentration in the mantle source, assumed equal to 0.3 wt %, D_o = the bulk initial crystal/melt partition coefficient for Na_2O, assumed equal to 0.03. The maximum melt fraction (F_o) in a unit column at the ridge axis was obtained by iteration for each MORB glass listed in Table 1. The mean degree of melting in this model is given by $<F>$ = $F_o/2$. The same model was developed by *Plank and Langmuir* [1992] and *Holness and Richter* [1989]. The corresponding initial depth Z_o and temperature T_o at which decompression melting begins is also shown, with resulting crustal thickness (D_c) (K&L'87). The relationships are $<F>$ = 0.006 $(P_o - P_f)$; $P_f = <F>^2/0.006$; $P_o = (<F>/0.006) + P_f = (<F> + <F>^2)/0.006$; $T_o = 1150 + 12\ P_o$; $D_c = 0.006(P_o - P_f)^2\ (10.2/\rho_c) = 648.56\ <F>^2\ P_o^{.038}$ (see Appendix in K&L'87) with P in kilobars, T in degrees Celsius and F as a fraction, and ρ_c is the density of the crust assumed to be 2.62 g/cm³. P_f = final pressure at which decompression melting stops at the base of the crust. P_o = the initial depth of melting. A mantle density of 3.3 g/cm³ was assumed to convert P_o into Z_o. Position of fracture zones and segment numbers used are also shown on top (see Figure 1 as well).

represent some of the deepest parts of the MAR axis over the entire Atlantic. Such great depths are matched only in the Arctic around 80°N and near the Bouvet triple junction around 55°S. The suggested minimum in crustal production at the ridge axis close to the St. Peter and Paul islets may thus partly explain the unusual exposure of mantle rocks on these islets. Exceptionally low mantle temperatures, initial pressures, and degrees of partial melting also occur at the east intersection of the Romanche transform with the ridge axis (east-RTI), which is highly fragmented in this region (Figure 1).

The relative patterns in T_o, and $<F>$ are extremely robust, but large uncertainties exist in the absolute values. Other parameterized melting models based on different major elements and assumptions give essentially the same spatial pattern of relative variation. For example, the model of *Niu and Batiza* [1991] based on a parameterization of Na_8, Ca_8/Al_8, and Fe_8/Si_8, an idealized flow model involving a finite melting column [*McKenzie and Bickle*, 1988], and a rather robust melting function, results in a potential mantle temperature profile essentially identical to that of the K&L'87 algorithm (Figure 11a). The parameterization of *Albarede* [1992], which is based on MgO and SiO_2, also produces a temperature profile similar to that calculated from the K&L'87 algorithm, although T_o is systematically lower by 100°-125°C (Figure 11b). In an attempt to define potential mantle temperature, degree of melting, and other melt production parameters in as general a way as possible, we have also considered other melting models [e.g., *Langmuir et al.*, 1992; *Kinzler and Grove*, 1993]. In absolute terms, a factor

of 2 discrepancy in $<F>$ and a direct shift of 125°C are apparent between these end-member melting models. It is not our purpose to evaluate the advantages, disadvantages, and uncertainties associated with each of these different melt production parameterizations. Rather, we emphasize that the application of each of these parameterized models to our petrologic data provides essentially the same relative along-ridge pattern of variations in melt production parameters. Finally, we note that the relative pattern of along-axis variations in mantle potential temperature and degree of melting derived from the analysis of MORB glasses is independently and qualitatively corroborated by variations in the mineral compositions of peridotites recovered in the study area [*Bonatti et al.*, 1992, 1993]. On this basis, Bonatti and colleagues suggested that the mantle beneath the equatorial Atlantic may be 150°C cooler than elsewhere along the MAR.

Passive Mantle Upwelling Model

The simplest hypothesis for the existence of the long-wavelength gradients in mantle melting parameters shown in Figure 10 is that the very long and densely distributed offset transforms at the equatorial MAR result in cooling of a large part of the upper mantle. To test this hypothesis, we applied the simple steady-state passive mantle upwelling model of *Phipps Morgan and Forsyth* [1988] to the specific geometry at the equatorial MAR. For the equatorial MAR the principal modification introduced to the standard model is an expansion of
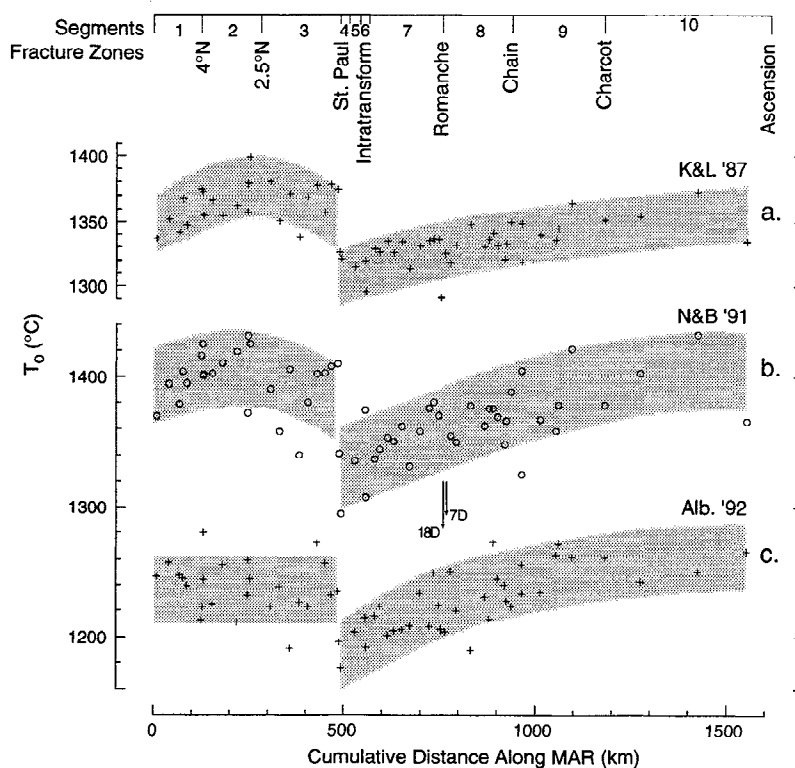

Figure 11. Variation of initial temperature of melting (T_o) in the mantle with cumulative distance along the MAR axis from 5°N. T_o is based on the equatorial MORB data of Table 1 averaged per station and the petrological decompression melting models of *Klein and Langmuir* [1987] (K&L'87), *Niu and Batiza* [1991] (N&B'91) and *Albarede* [1992] (Alb'92). Despite the fact that these models are based on different major elements and sets of assumptions, the relative patterns are very similar (though the absolute values may systematically differ by as much as 125°C, e.g., Alb'92 versus N&B's 91). The K&L'87 trend lies in between that of N&B'91 and Alb'92 trends. Note that a different scale is used for K&L'87.

the size of the solution grid. We assume an isoviscous mantle and wholly plate-driven (passive) flow and use a Fourier decomposition technique to determine mantle velocities throughout the lithosphere. The steady-state thermal structure of the lithosphere is calculated using an upwind finite differencing technique with constant temperature boundary conditions of 0°C and 1450°C at the surface and 100 km depth, respectively, and zero flux conditions from the sides of the box. Because our "plate" model assumes constant temperatures at a depth of 100 km, the cooling lithosphere can grow no thicker than 100 km. An alternative "half-space" cooling model would imply thicker cooling lithosphere everywhere and thus predict greater reduction on melting near transforms than our "plate" model. Note that we implicitly assume that passive upwelling driven by plate motions dominates mantle flow patterns near the ridge axis and that the present-day thermal regime can be approximated by a steady-state temperature solution.

The weakest assumption in our mantle flow model is that of a uniform thickness lithosphere. In the equatorial Atlantic the transform offsets are so large that the thin, hot lithosphere of the mid-ocean ridge system is sometimes juxtaposed against cool, thick lithosphere formed at 50 Ma (e.g., across the Romanche transform). The effects of changes in lithospheric thickness on mantle flow regimes and thermal structure have been explored in detail by *Lin and Parmentier* [1989] and *Blackman and Forsyth* [1992]. In these studies, the steady-state thermal regime calculated for the case of lithospheric thickening is generally similar to that determined for the constant lithospheric thickness case. The most important difference between the variable and constant lithospheric thickness models occurs near the ends of ridge segments adjacent to transform zones. At these sites, the along-axis temperature gradients are expected to be steeper and the zones of reduced melting narrower in thickening lithosphere models than in the constant lithospheric thickness models used here. It should be noted that, in the constant lithospheric thickness model, the horizontal conductive cooling of the lithosphere from a transform offset proceeds at about the same rate as cooling downward. Thus only ridge segments with lengths more than twice the lithospheric thickness will have a central area unaffected by the bounding transform offsets.

The steady-state temperature regime (see Figure 12c) determined from the passive flow model was used to calculate the depth to the base (initial melting) and top of the partial melting zone. For these calculations, we define the solidus function $T_s = 1150°C + 3.64z$, where z denotes depth in kilometers. As shown by the solid lines in Figure 12b, the top of partial melting zone lies at a depth of about 10 km in the center of each ridge segment and at greater depths at the ends of segments. The depth of initial melting (bottom of the melt zone) shows relatively little variation along the ridge axis, probably due to the constant temperature condition assumed at 100 km depth. The calculations reveal that little melt should be present near the ends of ridge segments adjacent to the large-offset St. Peter and Paul FZ and Romanche FZ. The region of reduced melt is asymmetric about the St. Peter and Paul FZ because relatively little melt is present beneath the intratransform spreading centers.

The average degree of fusion F curve (dotted line) in Figure 12b was calculated using the empirical liquidus relation of *McKenzie and Bickle* [1988] and the solidus function T_s just stated. The melt fraction at any depth is given by $[T(z)-T_s] / [T_l - T_s]$, and the average degree of melting was determined by integrating the melt fraction over depth within a zone up to 24 km wide centered on the ridge axis. Melt fractions within this zone

were only included in the averaging when the melt generation rate (given by the dot product of the flow velocity and the gradient of the melt fraction $<F>$) was positive. The partial melting function used is very similar to that of *Phipps Morgan and Forsyth* [1988], except that $(T_l - T_s)$ increases slightly with decreasing z in our model, instead of remaining constant at about 600°C. Assuming that 3% of melt is retained in the matrix, the passive flow model predicts average melt percent of 14.5% in the center of segments. The predicted average degree of melting decreases slightly near the ends of most segments and falls to 0% at the ends of ridge segments adjacent to the St. Peter and Paul FZ and the Romanche FZ.

Figure 12c shows the steady-state temperature structure at 13 km depth calculated using the passive flow model. Note particularly the low temperatures at the Romanche FZ and within the intratransform spreading centers in the St. Peter and Paul FZ. Although the variation in the melt production parameters along the transform zones is not seen in the along-axis profile in Figures 12a and 12b, the relatively cold temperatures within the St. Peter and Paul FZ and the Romanche FZ significantly affect melting and mantle conditions into adjacent ridge segments.

A comparison of the model results shown in Figure 12b to calculations of the same three parameters (initial and final depth of melting and average percent of melting) based on the petrologic decompression melting model of *Niu and Batiza* [1991] (Figure 12a) indicates that the cooling effect of the long transform offsets at the equatorial MAR is not adequate to produce the petrologically inferred long-wavelength mean degree of fusion gradient south of the St. Peter and Paul FZ. The apparent discontinuity in melt production parameters at the St. Peter and Paul FZ also cannot be matched using this simple passive flow model, which incorporates realistic ridge segment geometry and average spreading rate.

As noted above, thickening lithosphere would cause the average percent melting to remain at the midsegment value to nearly the ends of the segments, producing narrower zones of reduced melting near the ends of segments. Within the study area, the only two instances where such cold edge effects are petrologically apparent is at the Romanche east-RTI and to a lesser extent the Chain east-RTI. In both cases the cold edge effects are not apparent on the west-RTIs and therefore do not display the symmetrical pattern predicted by the passive flow model.

For the lithospheric thickening model, the maximum change in along-axis melting depth across the entire profile is expected to be the same or slightly larger than calculated for the constant lithospheric thickness passive flow model. It is therefore clear that, regardless of the specific passive flow model chosen, the observed long-wavelength gradient in melt production parameters cannot be explained merely by thermal effects related to large-offset fracture zones at the equatorial MAR. It should be emphasized that the goal of the thermal modeling calculations is not to match the petrologic data but rather to provide additional insights into the possible causes of the long-wavelength mantle temperature gradient inferred petrologically.

Discussion

There is little doubt that the discontinuity across the northernmost St. Paul transform fault and the peak in mantle temperature, degree of fusion, and crustal thickness inferred at 2°N is most likely caused by the Sierra Leone near-ridge plume. *Schilling et al.* [1994] have previously shown that this region is
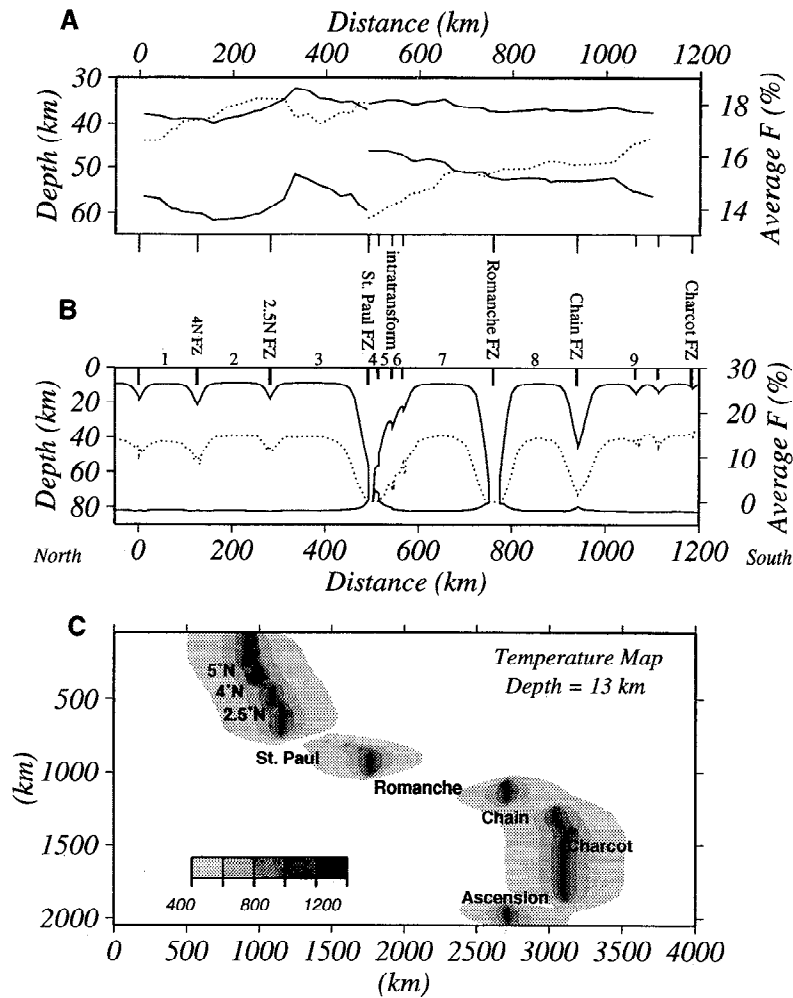
Figure 12. (a) Variation of initial and final depths of melting and corresponding mean degree of melting along the equatorial MAR axis (cumulative distance from 5°N), calculated using the MORB glass data of Table 1 and the *Niu and Batiza* [1991] petrologic decompression melting model. The Niu and Batiza model was chosen for comparison with the passive upwelling calculations since it provides initial and final depth of melting independently using $SiO_{2(8)}/FeO_{(8)}$ and $Na_2O_{(8)}$ combined with $CaO_{(8)}/Al_2O_{3(8)}$, respectively. A moving average with a 150-km-wide window was used to smooth the curves. (b) Results of the passive mantle upwelling model calculations. The solid lines show the depth of initial melting (~82 km within ridge segments) and final melting (~10 km within ridge segments) beneath the axis of the equatorial MAR (cumulative distance from 5°N). The dotted line marks the average degree of partial melting within a zone up to 24 km wide centered on the ridge axis. The method for calculating the degree of partial melting is discussed in the text. Note that no melt is predicted near the St. Peter and Paul and Romanche FZ. (c) Contour map (200° C contour interval) of the temperature distribution near the top of the zone of melting, at a depth of 13 km. These temperatures were determined using the passive mantle upwelling model of *Phipps Morgan and Forsyth* [1988]. The area filled with white has temperatures between 200°C and 400°C, and the ridge segments (black filled contour) have temperatures greater than 1200°C. Values indicated on the inset shading scale are in degrees Celcius.

underlain by a major radiogenic Nd, Sr, and Pb isotope and incompatible element rich anomaly. On the other hand, application of a steady-state passive flow model for determining the mantle thermal structure in the region shows that the compounding of cooling effects of the long transform offsets cannot be the sole cause of the large-scale gradient in mantle temperatures, crustal thickness, and mean degree of fusion inferred from the MORB glasses. This is paradoxical in light of the good correlations that exist among segment length, maximum along-ridge axis relief per segment, mean segment depth, and per segment average bulk composition of the erupted basalts and corresponding mean degrees of fusion (Figures 5-7). Either the

passive model considered is too simple or some other additional explanation for the petrologically inferred temperature gradient is required. We now briefly explore some alternative explanations.

1. The first possibility is that the major element and inferred upper mantle temperature gradient along the axis of the equatorial MAR may be caused by along-ridge subaxial pipe flow of the magma [e.g., *Vogt*, 1976]. It could conceivably be argued that the sign of the gradient in Mg #, $CaO/CaO+Na_2O$, Na_2O and $Cr/Cr+Al$ and along-axis depth (Figure 4) might reflect such a northward flow of melt which would be accompanied by cooling and increasing fractional crystallization from the Charcot to the St. Paul FZ. We rule out this hypothesis on several

grounds. First, in planform, the gradient shown in Figure 4 is not continuous, but rather disconnected by transform offsets reaching up to 900 km. The cold lithosphere juxtaposed against the ridge segments across such large offsets would clearly act as a barrier to flow. Furthermore, northward flow of melt would imply a flow direction toward, instead of away from, the zone influenced by the Sierra Leone plume. Such flow is inconsistent with the sign of the Pb-Sr-Nd isotope gradient observed near the Sierra Leone plume [see *Schilling et al.*, 1994].

2. A second hypothesis is that the cold area in the equatorial Atlantic might be related to either global or local patterns of mantle downwelling. For example, *Bonatti et al.* [1993] have suggested that the low in mantle temperature and percent fusion apparently present beneath the equatorial MAR may also be present beneath the equatorial regions of the Pacific and Indian oceans. In support of this contention, these workers invoke the apparent mid-ocean ridge axis depth minima present at the equator and previously documented by *Menard and Dorman* [1977]. On this basis, *Bonatti et al.* [1993] speculate that the inferred equatorial distribution of cold, dense upper mantle and DUPAL [named after *Dupré and Allègre*, 1983 by *Hart*, 1984] versus non-DUPAL isotopic mantle source domains may reflect widespread mantle downwelling beneath equatorial ocean basins. Such a pattern of downwelling concentrated at the equator is partially supported by mantle dynamics studies that predict a readjustment of Earth's rotation axis (true polar wander), and therefore its equator, in response to the downward movement of cold, high-density material through a mantle whose viscosity increases with depth [*Ricard et al.*, 1993]. True polar wander induced by the internal redistribution of mass results in changes in the nonhydrostatic component of degree 2 harmonic [*Spada et al.*, 1994]. Without additional constraints on long-wavelength variations in mantle thermal structure (e.g., from petrological/geochemical, tomographic, or other geophysical data), it would be premature to conclude that the cold areas in the equatorial MAR are part of a larger pattern of mantle downwelling concentrated near Earth's equator.

The question of distribution of mass and pattern of convection in the Earth is a complex issue [e.g., *Anderson*, 1989], which needs to be addressed more rigorously. In passing, we note that, in contrast to the Australian-Antarctic discordance (AAD), a locus of possible downwelling characterized by a major along-ridge isotopic discontinuity between so-called DUPAL type and Pacific-Atlantic type mantle source domains [*Klein et al.*, 1988; *Pyle et al.*, 1992], the equatorial Atlantic has no comparable isotopic discontinuity. Based on the MAR isotopic mapping of *Hanan et al.* [1986] and *Schilling et al.* [1994], such a large discontinuity, if it occurs at all in the Atlantic, would likely be located some 3000 km south of the study area, at about 24°S. Furthermore, we have previously interpreted the isotopic boundary in the south Atlantic not as a discontinuity separating DUPAL and Pacific-Atlantic mantle, but rather as a boundary between two distinct plume families and their influence in the asthenosphere: St. Helena type (non-DUPAL) and Tristan type (DUPAL) [*Hanan et al.*, 1986].

Localized downwelling might offer another explanation for the observed cold mantle region at the equatorial MAR. However, as pointed out to us by N. Sleep, downwelling along a normal adiabat does not change potential mantle temperatures. The petrologic data from the equatorial MAR clearly indicate that the mantle beneath this region must be colder than normal mantle. Thus even if local downwelling does occur in this area, some other process must be invoked to reduce mantle temperatures.

3. At this point we must consider a more local and immediate cause for the petrologically inferred cold spot and large-scale mantle temperature gradient present in the equatorial Atlantic south of the St. Peter and Paul FZ. Processes related to the nature and timing of opening of the equatorial Atlantic relative to the adjacent Atlantic basins may be one factor controlling the present-day mantle temperatures in this region. Differential opening in the Central Atlantic (~190 Ma) and South Atlantic (~130 Ma) was first accommodated along preexisting sutures and mobile belts on the eastern margin of the old (Archean-Proterozoic), cold, deep-rooted and rigid West African cratonic lithosphere [*Hurley and Rand*, 1969; *Burke and Dewey*, 1974; *Briden et al.*, 1981; *Fairhead*, 1988; *Lesquer and Vasseur*, 1992; *Nyblade and Pollack*, 1993b] (Figure 1). Between 110 Ma and 60 Ma, the initial phase of rifting and opening in the equatorial Atlantic occurred mostly in a strike-slip fashion [*Klitgord and Schouten*, 1986] along a probable leaky transform system between West African and South American continental lithosphere, both of which were probably unusually cold and thick (200-400km [e.g., *Briden et al.*, 1981; *Jordan*, 1988; *Yan et al.*, 1989]). Asthenospheric material, which passively upwelled between these two unusually deep and cold (cratonic) tectonospheric keels as they were displaced during rifting, is likely to have been cooled and subjected to small-scale convective overturn [*Yuen and Fleitout*, 1985; *Buck*, 1986; *Keen*, 1987a, b; *Nyblade and Pollack*, 1993a]. The small-scale nature of mantle heterogeneities in Pb-Nd-Sr isotopes observed south of the St. Paul FZ is suggestive of unusually intense convective and dispersal action [*Schilling et al.*, 1994]. The thin crust and highly sheared nature of the lithosphere may also have enhanced hydrothermal circulation, hydration, and, to some limited extent, the cooling of the asthenosphere from above. The possible occurrence of such processes is supported by the presence in the region of abundant outcrops of transverse serpentinized ridges, which are apparently older than the adjacent seafloor [*Bonatti and Honnorez*, 1971; *Bonatti*, 1973, 1978; *Bonatti et al.*, 1979]. Bonatti and his coworkers have emphasized the unusual character of opening and formation of seafloor in the equatorial Atlantic, including oscillatory spreading, rift propagation, shifts of transform faults, and compression and uplifts of so-called nonspreading, semistagnant, peridotitic blocks. Although some of these processes may represent normal responses to transtension accompanying plate boundary reorganization, there is evidence that unusual tectonic activity reaches as far as to the continental shelves of northern Brazil and the Ivory Coast [*Hayes and Ewing*, 1970; *Le Pichon and Hayes*, 1971; *Gorini and Bryan*, 1976].

4. The apparently cold nature of the upper mantle underlying the equatorial Atlantic might also be a reflection of longer-term and broader-scale convective phenomenon related to the aggregation and dispersal of supercontinents. In his time-dependent numerical simulation study, *Gurnis* [1988] has shown that, after a first dispersal, continents tend to aggregate over cold mantle downwelling regions. In this respect, it is interesting to note that the present equatorial region lies on the western fringe of the Atlantic–African residual geoid high and associated hotspot cluster discussed by *Anderson* [1982]. In the Jurassic configuration of continents, based on Morgan's hotspot based reconstruction, this mantle region would have been overlain by the western boundary of Pangea [*Anderson*, 1982]. The west-northwest strike of the 600-km-long upper mantle temperature gradient along the equatorial MAR axis (Figures 1 and 10) has the proper direction and sign expected for upper mantle

underlying such a continent/ocean transition zone some 200 m.y. ago. Thus the petrologically inferred upper mantle thermal anomaly beneath the equatorial Atlantic may well reflect such a longer term broad-scale mantle convective phenomenon.

This hypothesis, like hypothesis 3, implies that the cold mantle beneath the equatorial MAR cannot represent merely a localized cold spot. Since small cold spots will be thermally re-equilibrated on short timescales by conductive heating, long-lived thermal anomalies can only be explained by processes which affect a broader region. We envision such a region as having a scale intermediate between the long-wavelength downwellings favored by some mantle dynamics studies and the 2000-km-wide cold area inferred on the basis of petrologic data. It should also be noted that cold mantle material has negative buoyancy and normally sinks faster than it can be incorporated into patterns of passive upwelling beneath a mid-ocean ridge. Thus a relatively broad cold spot is required if some of this material is to have an opportunity to be entrained in the upward flow of mantle beneath the ridge axis, instead of merely sinking in the mantle. We caution that the use of the term "coldspot" does not imply that a cold region in the mantle can be replenished by the sort of upwelling processes similar to those that operate in hotspots.

Conclusions

In closing, we emphasize the following points:

1. To our knowledge, the regular, 600-km-long gradients in major elements from the equatorial Atlantic MORB glasses have so far not been observed at a similar large scale length at any other site along the global mid-ocean ridge system. The inference that such chemical gradients in the oceanic crust may reflect a similar gradient in the upper mantle temperature and melting conditions is quite robust and independent of the petrological models considered. Such gradients are particularly significant considering that the MAR in the equatorial Atlantic is highly segmented by very large transform fault offsets reaching up to 900 km (Romanche FZ). Although the cause of the petrologically inferred upper mantle cold zone remains uncertain and speculative, passive flow calculations show that it cannot be fully explained by the compounded cooling effects associated with these very long and densely distributed equatorial Atlantic transform offsets. Some other explanation needs to be sought in the past evolution of mantle in the region. We have briefly explored two such possibilities within the last 200 Ma history of the region, but these are poorly constrained and speculative.

2. Strong correlations exist between segment length and (1) maximum axial depth relief, (2) mean composition of equatorial MORBs, and (3) inferred magma budget (i.e., mean degree of melting, crustal thickness, etc.). We do not yet know whether the correlation among these morphotectonic, petrologic, and magma budget parameters indicate a dichotomy unique to the equatorial Atlantic or reflect an empirical correlation of greater significance to the global mid-ocean ridge system. Further examination of this question will require an integrated interpretation of Sea Beam bathymetry and gravity data and the petrologic results presented here.

3. Equatorial MORB glasses follow the K&L'87 global correlation of Na_8 with ridge elevation fairly well. However, Fe_8 does not conform to the K&L'87 global correlation and instead varies independently of Na_8. The observation is consistent with *Niu and Batiza's* [1993] conclusion that the sign of the Na_8 versus Fe_8 MORB correlation depends on spreading rate.

4. Extrapolation of the results of *Humler et al.* [1993], who noted a global correlation of Na_8 in MORBs to seismic S wave velocity tomographic imaging at 100 km depth, to the high Na_8 values found in the equatorial Atlantic would predict a 600-km-long gradient ranging from as high as +1% to -1% velocity variation from the Charcot FZ to the St. Paul FZ. A zone of high velocity in the upper mantle is also apparent over the equatorial Atlantic in the S wave tomographic results of *Woodhouse and Dziewonski* [1984] and *Zhang and Tanimoto* [1992]. Unfortunately, the resolution in these seismic tomography maps is insufficient to provide a reliable test of the petrologically inferred equatorial Atlantic coldspot hypothesis. However, based on such a correlation, the equatorial Atlantic mantle coldspot just south of St. Paul FZ is likely to be colder and seismically faster than mantle beneath the AAD, the Bouvet triple junction or the Cayman Trough, the deepest regions so far observed along the mid-ocean ridge system. Future detailed tomographic study of the equatorial Atlantic region is thus warranted.

5. The petrologic discontinuity across the complex St. Paul transform and the maxima in mantle temperature, degree of melting, crustal thickness, and associated high in Pb-Nd-Sr isotope found around 1.7°N most likely reflect the influence of the nearby Sierra Leone plume, which is located just east of the MAR [*Schilling et al.*, 1994].

6. In view of the petrologically inferred very low mantle temperature, thin crust, and highly fragmented nature of the ridge axis just south of the St. Paul FZ, it is perhaps not surprising that mantle rocks are exposed on St. Peter and St. Paul's islets. The extra buoyancy associated with the Sierra Leone plume is also likely to be an additional factor [*Schilling et al.*, 1994] contributing to the unroofing of these mantle rocks.

References

Albarede, F., How deep do common basaltic magmas form and differentiate?, *J. Geophys. Res.*, *97*, 10,997-11,009, 1992.

Anderson, D.L., Hotspots, polar wander, Mesozoic convection and the geoid, *Nature*, *297*, 391-393, 1982.

Anderson, D., *Theory of the Earth*, pp. 249-253, Blackwell Scientific, Cambridge, Mass., 1989.

Bender, J.F., C.H. Langmuir, and G.N. Hanson, Petrogenesis of basalt glasses from the Tamayo region, East Pacific Rise, *J. Petrol.*, *25*, 213-254, 1984.

Blackman, D.K., and D.W. Forsyth, The effects of plate thickening on three-dimensional, passive flow of the mantle beneath mid-ocean ridges, in *Mantle Flow and Melt Generation at Mid-Ocean Ridges*, *Geophys. Monogr. Ser.*, vol. 71, edited by J. Phipps Morgan, D.K. Blackman, and J.M. Sinton, pp. 311-326, AGU, Washington, D. C., 1992.

Bonatti, E., Origin of offsets of the Mid-Atlanic Ridge in fracture zones, *J. Geol.*, *81*, 144-156, 1973.

Bonatti, E., Vertical tectonism in oceanic fracture zones, *Earth Planet. Sci. Lett.*, *37*, 369-379, 1978.

Bonatti, E., and K. Crane, Oscillatory spreading explanation of anomalously old uplifted crust near oceanic transforms, *Nature, 300*, 343-345, 1982.

Bonatti, E., and J. Honnorez, Nonspreading crustal blocks at the Mid-Atlantic Ridge, *Science, 174*, 1329-1331, 1971.

Bonatti, E., A. Chermak, and J. Honnorez, Tectonic and igneous emplacement of crust in oceanic transform zones, in *Deep Drilling Results in the Atlantic Ocean: Ocean Crust, Maurice Ewing Ser.*, vol.2, edited by M. Talwani, C.G. Harrison, and D.E. Hayes, pp. 239-248, AGU, Washington, D. C., 1979.

Bonatti, E., A. Peyve, P. Kepezhinskas, N. Kurentsova, M. Seyler, S. Skolotnev, and G. Udintsev, Upper mantle heterogeneity below the Mid-Atlantic Ridge, 0°-15°N, *J. Geophys. Res., 97*, 4461-4476, 1992.

Bonatti, E., M. Seyler, and N. Sushevskaya, A cold suboceanic mantle belt at the Earth's equator, *Science, 261*, 315-320, 1993.

Briden, J.C., D.N. Whitcombe, G.W. Stuart, J.D. Fairhead, C. Dorbath, and L. Dorbath, Depth of geological contrast across the West African craton margin, *Nature, 292* , 123-128, 1981.

Brodholt, J.P., and R. Batiza, Global systematics of unaveraged mid-ocean ridge basalt compositions: Comment on"Global correlations of ocean ridge basalt chemistry with axial depth and crustal thickness" by E.M.Klein and C.H. Langmuir, *J. Geophys. Res., 94* , 4231-4239, 1989.

Buck, W.R., Small-scale convection induced by passive rifting: The cause for uplift of rift shoulders, *Earth Planet. Sci. Lett., 77*, 362-372, 1986.

Burke, K., and J.F. Dewey, Two plates in Africa during the Cretaceous?, *Nature, 249*, 313-316, 1974.

Detrick, R.S., and H.D. Needham, Variations in gravity, crustal thickness and morphology along the MAR between the Oceanographer and Hayes FZs (abstract), *Eos Trans. AGU, 73*(43), Fall Meting suppl., 568, 1992.

Dmitriev, L.V., A.V. Sobolev, and N.M. Suschevskaja, The primary melt of the oceanic tholeiite and the upper mantle composition, in *Deep Drilling Results in the Atlantic Ocean: Ocean Crust, Maurice Ewing Ser.*, vol. 2, edited by M. Talwani, C.G. Harrison, and D.E. Hayes, pp. 302-313, AGU, Washington, D. C., 1979.

Dupré, B., and C.J. Allègre, Pb-Sr isotope variation in Indian Ocean basalts and mixing phenomena, *Nature, 303*, 142-146, 1983.

Epp, D., and N.C. Smoot, Distribution of seamounts in the North Atlantic, *Nature, 337*, 254-257, 1989.

Fairhead, J.D., Mesozoic plate tectonic reconstructions of the central South Atlantic Ocean: The role of the West and Central African rift system, *Tectonophysics, 155*, 181-191, 1988.

Fairhead, J.D., and C.M. Green, Controls on rifting in Africa and the regional tectonic model for the Nigeria and East Niger rift basins, *J. Afr. Earth Sci., 8*(2-4), 231-249, 1989.

Forsyth, D.W., and B. Wilson, Three-dimensional temperature structure of a ridge-transform-ridge system, *Earth Planet. Sci. Lett., 70*, 355-362, 1984.

Fox, P.J., and D.G. Gallo, A tectonic model for ridge-transform-ridge plate boundaries: Implications for the structure of oceanic lithosphere, *Tectonophysics, 104*, 205-242, 1984.

Frey, F.A., Rare earth and potassium abundances in St. Paul's Rocks, *Earth Planet. Sci. Lett., 7*, 351-360, 1970.

Gorini, M.A., and G.M. Bryan, The tectonic fabric of the equatorial Atlantic and adjoining continental margins: Gulf of Guinea to Northeastern Brazil, *An. Acad. Bras. Ciênc., 48*, Suppl., 101-119, 1976.

Gurnis, M., Large-scale mantle convection and the aggregation and dispersal of supercontinents, *Nature, 332*, 695-699, 1988.

Hanan, B.B., R.H. Kingsley, and J.-G. Schilling, Pb isotope evidence in the South Atlantic for migrating ridge-hotspot interactions, *Nature, 322*, 137-144, 1986.

Hart, S.R., A large-scale isotope anomaly in the Southern Hemisphere mantle, *Nature, 309*, 753-757, 1984.

Hayes, D.E., and M. Ewing, North Brazilian Ridge and adjacent continental margin, *Amer. Assoc. Petrol. Geol. Bull., 54*, 2120-2150, 1970.

Holness, M.B., and F.M. Richter, Possible effects of spreading rate on

MORB isotopic and rare earth composition arising from melting of a heterogeneous source, *J. Geol., 97*, 247-260, 1989.

Honnorez, J., and E. Bonatti, Nepheline gabbro from the Mid-Atlantic Ridge, *Nature, 228*, 850-852, 1970.

Humler, E., J.L. Thirot, and J.P. Montagner, Global correlations of mid-ocean-ridge basalt chemistry with seismic tomographic images, *Nature, 364*, 225-228, 1993.

Hurley, P.M., and J.R. Rand, Pre-drift continental nuclei, *Science, 164*, 1229-1242, 1969.

Jordan, T.H., Structure and formation of the continental tectosphere, *J. Petrol. Special Lithosphere Issue*, 11-37, 1988.

Keen, C.E., Dynamical extension of the lithosphere during rifting: Some numerical model results, in *Composition, Structure and Dynamics of the Lithosphere-Asthenosphere System, Geodyn. Ser.*, vol. 16, edited by K. Fuchs and C. Froidevaux, pp. 189-203, AGU, Washington, D. C., 1987a.

Keen, C.E., Some important consequences of lithospheric extension, in *Continental Extensional Tectonics*, edited by M.P. Coward, J.F. Dewey, and P.L. Hancock, pp. 67-73, Blackwell Scientific, Boston, Mass., 1987b.

Kinzler, R.J., and T.L. Grove, Primary magmas of mid-ocean ridge basalts, 1, Experiments and results, *J. Geophys. Res., 97*, 6885-6906, 1992a.

Kinzler, R.J., and T.L. Grove, Primary magmas of mid-ocean ridge basalts, 2, Applications, *J. Geophys. Res., 97*, 6907-6926, 1992b.

Kinzler, R.J., and T.L. Grove, Corrections and further discussion of the primary magmas of mid-ocean ridge basalts, 1 and 2, *J. Geophys. Res., 98*, 22,339-22,347, 1993.

Klein, E.M., and C.H. Langmuir, Global correlations of ocean ridge basalt chemistry with axial depth and crustal thickness, *J. Geophys. Res., 92*, 8089-8115, 1987.

Klein, E.M., and C.H. Langmuir, Local versus global variations in ocean ridge basalt composition: A reply, *J. Geophys. Res., 94*, 4241-4252, 1989.

Klein, E.M., C.H. Langmuir, A. Zindler, H. Staudigel, and B. Hamelin, Isotope evidence of a mantle convection boundary at the Australian-Antarctic discordance, *Nature, 333*, 623-629, 1988.

Klein, E.M., C.H. Langmuir, and H. Staudigel, Geochemistry of basalts from the southeast Indian Ridge, 115°E-138°E, *J. Geophys. Res., 96*, 2089-2107, 1991.

Klitgord, K.D., and H. Schouten, Plate kinematics of the central Atlantic, in *The Geology of North America*, edited by P.R. Vogt and B.E. Tucholke, pp. 351-378, Geological Society of America, Boulder, Colo., 1986.

Kuo, B.Y., and D.W. Forsyth, Gravity anomalies of the ridge-transform system in the South Atlantic between 31 and 34.5°S: Upwelling centers and variations in crustal thickness, *Mar. Geophys. Res., 10*, 205-232, 1988.

Langmuir, C.H., and J.F. Bender, The geochemistry of oceanic basalts in the vicinity of transform faults: Observations and implications, *Earth Planet. Sci. Lett., 69*, 107-127, 1984.

Langmuir, C.H., E.M. Klein, and T. Plank, Petrological systematics of Mid-Ocean Ridge basalts: Constraints on melt generation beneath ocean ridges, in *Mantle Flow and Melt Generation at Mid-Ocean Ridges, Geophys. Monogr. Ser.*, vol. 71, edited by J. Phipps Morgan, D.K. Blackman, and J.M. Sinton, pp. 183-280, AGU, Washington, D. C., 1992.

Le Pichon, X., and D.E. Hayes, Marginal offsets, fracture zones, and the early opening of the South Atlantic, *J. Geophys. Res., 76*, 6283-6293, 1971.

Le Roex, A.P., H.J.B. Dick, and R.L. Fisher, Petrology and geochemistry of MORB from 25°E to 46°E along the southwest Indian Ridge: Evidence for contrasting styles of mantle enrichment, *J. Petrol., 30*, 947-986, 1989.

Lesquer, A., and G. Vasseur, Heat-flow constraints on the west African lithosphere structure, *Geophys. Res. Lett., 19*, 561-564, 1992.

Lin, J., and E.M. Parmentier, Mechanisms of lithospheric extension at mid-ocean ridges, *Geophys. J., 96*, 1-22, 1989.

Lin, J., G.M. Purdy, H. Schouten, J.-C. Sempere, and C. Zervas, Evidence

for focused magmatic accretion along the Mid-Atlantic Ridge, *Nature*, *344*, 627-632, 1990.

Mahalanobis, P.C., On the generalized distance in statistics, *Proc. Nat. Inst. Sci. India*, *12*, 49-55, 1936.

McKenzie, D.P., and M.J. Bickle, The volume and composition of melt generated by adiabatic upwelling, *J. Petrol.*, *29*, 625-679, 1988.

Melson, W.G., E. Jarosewich, V.T. Bowen, and G. Thompson, St. Peter and St. Paul Rocks: A high-temperature, mantle-derived intrusion, *Science*, *155*, 1532-1535, 1967a.

Melson, W.G., and T. O'Hearn, Basaltic glass erupted along the Mid-Atlantic Ridge between 0-37°N: Relationships between composition and latitude, in *Deep Drilling Results in the Atlantic Ocean: Ocean Crust, Maurice Ewing Ser.*, vol. 2, edited by M. Talwani, C.G. Harrison, and D.E. Hayes, pp. 273-284, AGU, Washington, D. C., 1979.

Melson, W.G., and G. Thompson, Glassy abyssal basalts, Atlantic sea floor near St. Paul's Rocks: Petrography and composition of secondary clay minerals, *Geol. Soc. Am. Bull.*, *84*, 703-716, 1973.

Melson, W.G., E. Jarosewich, and R. Cifelli, Alkali olivine basalt dredged near St. Paul's Rocks, Mid-Atlantic Ridge, *Nature*, *215*, 381-382, 1967b.

Melson, W.G., S.R. Hart, and G. Thompson, St. Paul's Rocks, equatorial Atlantic: Petrogenesis, radiometric ages, and implications on sea-floor spreading, *Mem. Geol. Soc. Am.*, *132*, 241-272, 1972.

Menard, H.W., and L.M. Dorman, Dependence of depth anomalies upon latitude and plate motion, *J. Geophys. Res.*, *82*, 5229-5335, 1977.

Niu, Y., and R. Batiza, An empirical method for calculating melt compositions produced beneath mid-ocean ridges: Application for axis and off-axis (seamounts) melting, *J. Geophys. Res.*, *96*, 21,753-21,777, 1991.

Niu, Y., and R. Batiza, Chemical variation trends at fast and slow spreading mid-ocean ridges, *J. Geophys. Res.*, *98*, 7887-7902, 1993.

Nyblade, A.A., and H.N. Pollack, A comparative study of parameterized and full thermal-convection models in the interpretation of heat flow from cratons and mobile belts, *Geophys. J. Int.*, *113*, 747-751, 1993a.

Nyblade, A.A., and H.N. Pollack, A global analysis of heat flow from Precambrian terrains: Implications for the thermal structure of Archean and Proterozoic lithosphere, *J. Geophys. Res.*, *98*, 12,207-12,218, 1993b.

Parmentier, E.M., and D.W. Forsyth, Three-dimensional flow beneath a slow spreading ridge axis: A dynamical contribution to the deepening of the median valley toward fracture zones, *J. Geophys. Res.*, *90*, 678-684, 1985.

Parson, L.M., and R.C. Searle, Strike-slip fault styles in slow-slipping oceanic transform faults - Evidence from GLORIA surveys of Atlantis and Romanche fracture zones, *J. Geol. Soc. London*, *143*, 757-761, 1986.

Phipps Morgan, J., and D.W. Forsyth, Three-dimensional flow and temperature perturbations due to a transform offset: Effects on oceanic crustal and upper mantle structure, *J. Geophys. Res.*, *93*, 2955-2966, 1988.

Plank, T., and C.H. Langmuir, Effects of the melting regime on the composition of the oceanic crust, *J. Geophys. Res.*, *97*, 19,749-19,770, 1992.

Pouchou, J.-P., and F. Pichoir, Basic expression of "PAP" computation for quantitative EPMA, in *11th International Congress on X-ray Optics and Microanalysis*, edited by J.D. Brown and R.H. Packwood, pp. 249-253, Graphic Services, University of Western Ontario, London, Ont., 1987.

Prince, R.A., and D.W. Forsyth, Horizontal extent of anomalously thin crust near the Vema fracture zone from the three-dimensional analysis of gravity anomalies, *J. Geophys. Res.*, *93*, 8051-8063, 1988.

Pyle, D.G., D.M. Christie, and J.J. Mahoney, Resolving an isotopic boundary within the Australian-Antarctic Discordance, *Earth Planet. Sci. Lett.*, *112*, 161-178, 1992.

Ricard, Y., G. Spada, and R. Sabadini, Polar wandering for a dynamic Earth, *Geophys. J. Int.*, *113*, 284-298, 1993.

Roden, M.K., S.R. Hart, F.A. Frey, and W.G. Melson, Sr, Nd and Pb isotopic and REE geochemistry of St. Paul's Rocks: The metamorphic and metasomatic development of an alkali basalt mantle source, *Contrib. Mineral. Petrol.*, *85*, 376-390, 1984.

Schilling, J.-G., and H. Sigurdsson, Thermal minima along the axis of the Mid-Atlantic Ridge, *Nature*, *282*, 370-375, 1979.

Schilling, J.-G., M. Zajac, R. Evans, T. Johnston, W. White, J.D. Devine, and R. Kingsley, Petrologic and geochemical variations along the Mid-Atlantic Ridge from 29°N to 73°N, *Am. J. Sci.*, *283*, 510-586, 1983.

Schilling, J.-G., B.B. Hanan, B. McCully, and R.H. Kingsley, Influence of the Sierra Leone mantle plume on the equatorial Mid-Atlantic Ridge: A Nd-Sr-Pb isotopic study, *J. Geophys. Res.*, *99*, 12,005-12,028, 1994.

Schouten, H., K.D. Klitgord, and H.J.B. Dick, Migration of mid-ocean ridge volcanism, *Nature*, *317*, 225-229, 1987.

Shaw, D.M., Trace element fractionation during anatexis, *Geochim. Cosmochim. Acta*, *34*, 237-243, 1970.

Sigurdsson, H., First-order major element variation in basalt glasses from the Mid-Atlantic Ridge: 29°N to 73°N, *J. Geophys. Res.*, *86*, 9483-9502, 1981.

Sinton, J.M., Ultramafic inclusions and high-pressure xenocrysts in submarine basanitoid, equatorial Mid-Atlantic Ridge, *Contrib. Mineral. Petrol.*, *70*, 49-57, 1979.

Sleep, N.H., Tapping of magmas from ubiquitous mantle heterogeneities, an alternative to mantle plumes?, *J. Geophys. Res.*, *89*, 10,029-10,041, 1984.

Sleep, N.H., and S. Biehler, Topography and tectonics at the intersections of fracture zones with central rifts, *J. Geophys. Res.*, *75*, 2748-2752, 1970.

Spada, G., R. Sabadini, and E. Boschi, True polar wander affects the Earth dynamic topography and favours a highly viscous lower mantle, *Geophys. Res. Lett.*, *21*, 137-140, 1994.

Thompson, G., and W.G. Melson, The petrology of oceanic crust across fracture zones in the Atlantic Ocean: Evidence of a new kind of sea-floor spreading, *J. Geol.*, *80*, 526-538, 1972.

Thompson, G., W.B. Bryan, and W.G. Melson, Geological and geophysical investigation of the Mid-Cayman Rise Spreading Center: Geochemical variation and petrogenesis of basalt glasses, *J. Geol.*, *88*, 41-55, 1980.

Van Andel, T.H., J.D. Phillips, and R.P. Von Herzen, Rifting origin for the Vema fracture in the North Atlantic, *Earth Planet. Sci. Lett.*, *5*, 296-300, 1969.

Vogt, P.R., Plumes, subaxial pipe flow, and topography along the mid-oceanic ridge, *Earth Planet. Sci. Lett.*, *29*, 309-325, 1976.

White, R.S., R.S. Detrick, M.C. Sinha, and M.H. Cormier, Anomalous seismic crustal structure of oceanic fracture zones, *Geophys. J. R. Astron. Soc.*, *79*, 779-798, 1984.

Woodhouse, J.H., and A.M. Dziewonski, Mapping the upper mantle: Three-dimensional modeling of Earth structure by inversion of seismic waveforms, *J. Geophys. Res.*, *89*, 5953-5986, 1984.

Yan, B., E.K. Graham, and K.P. Furlong, Lateral variations in upper mantle thermal structure inferred from three-dimensional seismic inversion models, *Geophys. Res. Lett.*, *16*, 449-452, 1989.

Yoder, H.S.J., and C.E. Tilley, Origin of basalt magmas: An experimental study of natural and synthetic rock systems, *J. Petrol.*, *3*, 342-532, 1962.

Yuen, D.A., and L. Fleitout, Thinning of the lithosphere by small-scale convective destabilization, *Nature*, *313*, 125-128, 1985.

Zhang, Y.-S., and T. Tanimoto, Ridges, hotspots and their interaction as observed in seismic velocity maps, *Nature*, *355*, 45-49, 1992.

A. N. Davis, Cameca Instrument Inc., 204 Spring Hill Road, Trumbull, CT 06611.

R. H. Kingsley, B. McCully, J.-G. Schilling, and S. A. Tighe, University of Rhode Island, Graduate School of Oceanography, South Ferry Road, Narragansett, R.I. 02882. (email: jgs@gsosun1.gso.uri.edu)

J. Lin, Woods Hole Oceanographic Institution, Woods Hole, MA 02543.

C. Ruppel, School of Earth and Atmospheric Sciences, Georgia Institute of Technology, Atlanta, GA 30332-0340.